Progress in Oceanography 239 (2025) 103578

Contents lists available at ScienceDirect

Progress in Oceanography

journal homepage: www.elsevier.com/locate/pocean

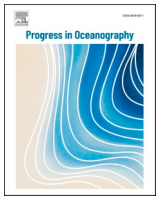

Holocene oceanographic variability in the Subtropical Northeast Atlantic☆

Irene Pérez-Rodríguez [a,*], Dirk Nürnberg [b], Julie C. Schindlbeck-Belo [b], Jack H. Wharton [c], Thor H. Hansteen [b], Veerle A.I. Huvenne [d,e], David J.R. Thornalley [c], Ángela Mosquera Giménez [f], Steffen Kutterolf [b], Kelsey Archer Barnhill [g], Covadonga Orejas [e,h]

[a] Centro Oceanográfico de Vigo, Instituto Español de Oceanografía, IEO-CSIC, Vigo, Spain
[b] GEOMAR Helmholtz Centre for Ocean Research, Kiel, Germany
[c] Department of Geography, University College London, United Kingdom
[d] National Oceanography Centre, Southampton, United Kingdom
[e] Hanse-Wissenschaftskolleg Institute for Advanced Study, Delmenhorst, Germany
[f] Centro Oceanográfico de Canarias, Instituto Español de Oceanografía, IEO-CSIC, Santa Cruz de Tenerife, Spain
[g] School of GeoSciences, University of Edinburgh, Edinburgh, United Kingdom
[h] Centro Oceanográfico de Gijón, Instituto Español de Oceanografía, IEO-CSIC, Gijón, Spain

ARTICLE INFO

Keywords:
Holocene
Planktonic foraminifera
Cabo Verde Archipelago
Northwest Africa upwelling
North Atlantic Subtropical Gyre
Tephra

ABSTRACT

Cabo Verde hosts unique, highly biodiverse marine ecosystems that thrive on volcanic seamounts and island slopes. These ecosystems are shaped by distinct oceanographic dynamics, influenced by the southeastern edge of the North Atlantic Subtropical Gyre (NASTG) and by seasonal upwelling. To explore regional oceanographic variability over time, this study investigates Holocene (last 11.7 ka) sediments using multi-proxy palaeoenvironmental reconstructions from a short core retrieved from ~ 4,400 m water depth off Cabo Verde.

During the Early Holocene, year-round upwelling, or an intensified Guinea Dome, may have inhibited the development of the strong summer stratification characteristic of the modern regional non-upwelling season. Despite humid conditions over the continent, sea surface temperatures (SSTs) remained relatively low during this subepoch, diverging from the present-day pattern in Northwest Africa, where the wet season is marked by weaker upwelling and higher SSTs. This oceanographic state was likely driven by precession-induced insolation changes associated with the precession minimum, which may have modified seasonal regional wind regimes and influenced broader atmospheric processes. Teleconnections related to transitional postglacial conditions and/or continental climate feedbacks, may also have played a role. The Middle Holocene, corresponding to the most humid conditions of this epoch in Northwest Africa, is characterized by reduced upwelling and an eastward expansion of the NASTG, inferred from warmer subsurface conditions at our study site. This interval also provides tentative evidence for enhanced input of North Atlantic Deep Water (NADW) into the Northeast Atlantic Bottom Water (NEABW). During the Late Holocene, intensified upwelling and a reduced influence of the NASTG, possibly due to a westward retraction of its eastern boundary, are suggested at our site, occurring under arid conditions in Northwest Africa.

These results highlight that, despite the overall climatic stability of the Holocene, oceanographic conditions off Cabo Verde experienced significant changes in seasonal upper ocean stratification, upwelling, subtropical gyre influence, and deep-water structure. Such insights improve our understanding of regional climate-ocean interactions, helping to refine climate models and improve predictions of ecosystem responses in this sensitive marine region.

☆ This article is part of a special issue entitled: 'Cabo Verde marine ecosystem' published in Progress in Oceanography.

* Corresponding author.
E-mail address: irene.perez@ieo.csic.es (I. Pérez-Rodríguez).

https://doi.org/10.1016/j.pocean.2025.103578

Available online 27 September 2025
0079-6611/© 2025 The Author(s). Published by Elsevier Ltd. This is an open access article under the CC BY license (http://creativecommons.org/licenses/by/4.0/).

1. Introduction

The Holocene, spanning the last 11.7 ka, is traditionally considered a relatively stable climatic epoch, particularly when contrasted with the dramatic climatic variations of the Quaternary period. It is formally subdivided into three subepochs (Walker et al., 2019): the Early Holocene (from 11.7 ka BP to 8.2 ka BP), the Middle Holocene (from 8.2 ka BP to 4.2 ka BP), and the Late Holocene (from 4.2 ka BP to the present). Nevertheless, several processes still modulated Holocene environmental variability. Climate shifts were influenced by half- and quarter-precession cycles, which cause differences in summer insolation between the hemispheres (e.g., Billups and Scheinwald, 2014; Ferretti et al., 2015; McIntyre and Molfino, 1996; Weirauch et al., 2008). These precession insolation changes have been linked to the occurrence of African Humid Periods (AHPs), recurring humid phases in North Africa that led to the expansion of savannah across the Sahara (e.g., Armstrong et al., 2023; deMenocal et al., 2000a, 2000b; Larrasoaña et al., 2013). AHPs are associated with precession minima, which increase summer insolation in the Northern Hemisphere, resulting in heating over the continent and the formation of a low-pressure zone over the Sahara and Sahel regions. This weakens the trade winds, facilitates the influx of moisture-laden air, and intensifies the African monsoon system (Biasutti, 2019; Blanchet et al., 2013). At the same time, the Intertropical Convergence Zone (ITCZ), the band of low atmospheric pressure formed by the convergence of trade winds from both hemispheres, shifts northward (Armstrong et al., 2023). The most recent AHP occurred during the Early and Middle Holocene, although hydrological reconstructions show heterogeneous timing (e.g., Kröpelin et al., 2008; Kuper and Kröpelin, 2006; Liu et al., 2017).

In addition to atmospheric reorganisation, precession variations induced major changes in low-latitudes stratification in the Atlantic during the Holocene (Billups and Scheinwald, 2014; Flores et al., 2000; McIntyre and Molfino, 1996; McIntyre et al., 1989; Nascimento et al., 2021; Venancio et al., 2018; Wolff et al., 1999). The seasonal migration of the ITCZ in this region serves as a modern analogue for the long-term effects of precession on atmospheric and upper ocean structure. In boreal winter, the ITCZ shifts closer to the equator. This intensifies easterly trade winds and enhances upwelling off the northwest African coast, leading to surface cooling, higher nutrient availability, and the development of a shallow seasonal thermocline (Hernández-Guerra et al., 2002). In summer, when the ITCZ is situated at approximately 20°N, the heavy African rainy season (summer monsoon) prevails, and a deeper thermocline develops in the Subtropical East Atlantic.

However, annual fluctuations are insufficient analogues for longer orbital periods (McIntyre et al., 1989). The complex interplay among different climate processes is illustrated by the fact that rainfall over Africa does not depend solely on the dynamics of the ITCZ and other mid- and high- tropospheric processes, including the dynamics of the African Easterly Jet, strongly influence the extension, position and strength of the rain belt (Armstrong et al., 2023; Collins et al., 2011; Matsuzaki et al., 2011; Zarriess and Mackensen, 2010). Additionally, global-scale phenomena also contribute to variability in upwelling and rainfall. For instance, Yamoula et al. (2025) show that upwelling off Mauritania and Senegal is strongly influenced not only by regional wind conditions, but also by the El Niño-Southern Oscillation (ENSO), the coupled ocean–atmosphere phenomenon characterised by anomalous variability in sea surface temperatures (SSTs) in the eastern tropical Pacific. In particular, strong La Niña events are associated with an increase in upwelling intensity in the region. Furthermore, Rodríguez-Fonseca et al. (2015) demonstrate that Sahel rainfall is sensitive to SST anomalies not only in the Atlantic, but also in the Pacific and Indian Oceans, as well as the Mediterranean Sea.

This complexity continues to hinder a full understanding and accurate representation of AHPs in climate models (e.g., Dallmeyer et al., 2020; Hopcroft et al., 2021; Pausata et al., 2020), and contributes to the ongoing uncertainty about the role of the ocean in the greening of the Sahara (Gaetani et al., 2024). In this context, other atmospheric and oceanographic processes have also been proposed to influence the last AHP, alongside the northward shift of the ITZC driven by insolation changes and the impact of the West African Monson. These include an increased contribution of winter moisture from the Mediterranean Sea (Cheddadi et al., 2021), shifts in the North Atlantic Oscillation (NAO) from predominantly positive to neutral-to negative phases in winter and summer, and a westward shift in the global Walker circulation (Gaetani et al., 2024). In addition, various processes involving feedback mechanisms may have contributed to the development of vegetation during the AHP (Chandan and Peltier, 2020; Pausata et al., 2016; Swann et al., 2014).

Furthermore, understanding oceanic changes at low latitudes during the Holocene is crucial for comprehending atmosphere–ocean teleconnections with higher latitudes, as environmental shifts in the Subtropics are linked to broader North Atlantic dynamics (deMenocal et al., 2000b; Mulitza et al., 2008; Nakanishi et al., 2021; Reißig et al., 2019). The deglacial meltwater input to the North Atlantic concluded with the demise of the Laurentide Ice Sheet at ~ 7 ka BP (Carlson et al., 2008; Gregoire et al., 2018), coinciding with a rearrangement of North Atlantic deep water formation toward a more modern-like setting (Hillaire-Marcel et al., 2001; Hoogakker et al., 2011), a major reorganization of surface ocean circulation at 7–8 ka BP (Thornalley et al., 2010), and changes in the North Atlantic gyres (Cléroux et al., 2012; Reißig et al., 2019; Repschläger et al., 2017).

On shorter timescales within the Holocene, multi-centennial cold events are superimposed on precession-driven changes. These events may be linked to solar cycles, clusters of volcanic eruptions, or internal oscillations within the ocean-climate system. They have been associated with changes in the subpolar North Atlantic and, through teleconnections, with global climate shifts (Bond et al., 2001; Mayewski et al., 2004; Moffa-Sánchez and Hall, 2017; Thornalley et al., 2009; Wanner et al., 2011).

The aim of this research is to investigate the Holocene ocean and climate variability on a centennial to millennial timescale in the northeastern subtropical Atlantic region, with a particular focus on water column structure and circulation changes. By examining these oceanic signals in a region influenced by the AHP and subsequent Saharan desertification, we explore potential links between ocean conditions and hydroclimate variability in Northwest Africa. Our study area encompasses (1) the highly productive upwelling off the west African coast, which is vital for regional marine ecosystems and many fishery-dependent communities, (2) the North Atlantic Subtropical Gyre (NASTG), which recirculates warm water and nutrients between 10°N and 40°N, an ideal setting to track variations in the spatial reach of gyre-influenced water masses, and (3) interactions between the deeper water masses at the site, including the Northeast Atlantic Bottom Water (NEABW) and the Antarctic Bottom Water (AABW), both of which with important roles in global ocean circulation.

To investigate Holocene climate variability in the eastern subtropical gyre, we analysed sediments from a marine core extracted from the abyssal plain off southwest Cabo Verde, taking a multidisciplinary, multi-proxy approach. First, we characterised the sediment composition, which included an inventory and classification of tephra, a distinction between marine and terrigenous inputs, and the identification of proxies of either arid or humid climatic conditions. Second, we reconstructed the vertical characteristics and structure of the upper ocean, which provided insights into upwelling and the influence of the NASTG. Third, we conducted a preliminary assessment of bottom water properties to explore the geochemical evolution of the NEABW and its potential interactions with AABW.

This study contributes to our understanding of long-term oceanographic dynamics, which is important for predicting how marine ecosystems might be impacted by future oceanographic scenarios (e.g., Henry et al., 2014). Evidence suggests that oceanographic conditions in the region may already be shifting due to ongoing global climate change,

with upwelling rapidly increasing during the 20th century and potentially continuing to intensify (García-Reyes et al., 2015; McGregor et al., 2007). However, projections of future changes remain highly uncertain due to the complex interplay between regional and large-scale drivers, and responses may vary across different areas of the upwelling system (Sarre et al., 2024). These findings underscore the importance of continued research to refine our understanding of oceanographic dynamics in this area.

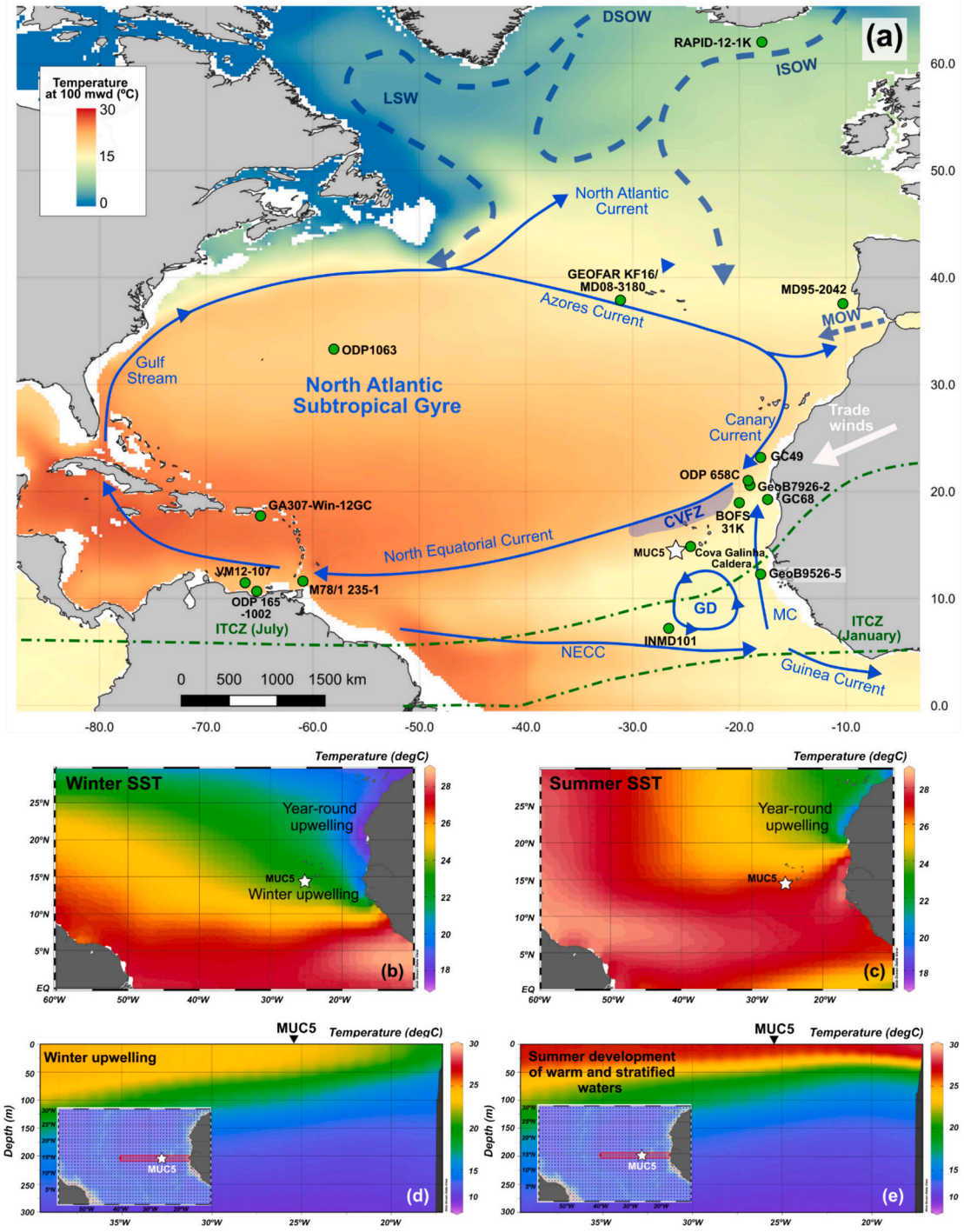

Fig. 1. North Atlantic subsurface hydrological setting, with the schematic oceanographic pattern of the area and seasonal sea surface temperatures (SSTs) presented as surface maps and water temperature variations along vertical sections. The location of the MUC5 sediment core is marked by a white star, while green dots represent the reference sites. (a) Modern temperatures at 100 m water depth and surface currents (blue arrows): NECC = North Equatorial Counter Current; MC = Mauritanian Current. The North Atlantic Subtropical Gyre (NASTG) and the Guinea Dome (GD) are indicated with blue circles, and the Cabo Verde Frontal Zone (CVFZ) is represented by blue shading. Deep water masses are indicated with dashed blue thick lines: LSW = Labrador Sea Water; DSOW = Denmark Strait Overflow Water; ISOW = Iceland-Scotland Overflow Water; MOW = Mediterranean Outflow Water. A white arrow schematically illustrates the direction of the prevailing trade winds, and green dotted lines indicate the Intertropical Convergence Zone (ITCZ) during two different seasons. (b) Modern surface temperatures in winter (January-March) and (c) summer (July-September). (d) Vertical temperature structure in the upper 300 m of the ocean during winter (January-March), and (e) summer (July-September). Maps and profiles sourced from Ocean Data View (Schlitzer and Mieruch-Schnülle, 2024) and World Ocean Atlas (WOA) (Reagan et al., 2024).

2. Regional setting

The study site is situated in the Cabo Verde Basin, southwest of the Cabo Verde archipelago (Fig. 1a), within a dynamic oceanographic transition zone influenced by seasonal upwelling (Fig. 1b-e), as well as by regional hydrographic features such as the NASTG (Fig. 2a-c) and the Guinea Dome (Fig. 2d).

Northeasterly trade winds, which consistently blow over the area, significantly influence the following main regional oceanographic and environmental processes:

Coastal upwelling off Northwest Africa: This wind-driven upwelling is one of the most biologically productive regions in the world (Pauly and Christensen, 1995). While upwelling is sustained throughout the year north of 20°N, in the region south of this latitude, where the Cabo Verde Basin is located, upwelling occurs primarily between late fall and early spring (Cropper et al., 2014; Valdés and Déniz-González, 2015). This seasonal upwelling coincides with the enhanced influence of the easterly winds in the area due to their winter southward migration. The main present-day seasonal variations in SST down to 150 m water depth are associated with the development of the Northwest African coastal upwelling system (Fig. 1b-e).

Surface ocean currents: The study area is mostly influenced by the North Equatorial Current (NEC), which flows westward north of the archipelago, constituting the south-eastern edge of the NASTG (Fig. 1a; Fig. 2a-c). In contrast to the more seasonally variable upper layers (Fig. 1d-e), the subsurface thermal structure is relatively stable throughout the year and reflects the typical eastward extent of the NASTG, as illustrated by the temperature distribution at 275 m depth in Fig. 2c. Additionally, the North Equatorial Countercurrent (NECC) flows eastward along the equator, and lies to the south of the archipelago (Fig. 1a). During boreal summers, the opposing flows of these two currents induce a cyclonic circulation pattern resulting in the formation of the Guinea Dome (Mazeika, 1967), which marginally affects the site (Fig. 2d). This oceanographic feature has its centre at ~ 10°N and ~ 22°W and is characterised by an uplift of the isotherms, particularly prominent at around 50 m water depth. This Dome enhances regional productivity (Fernández-Carrera et al., 2023) and could influence rainfall patterns over the tropical Atlantic, particularly affecting northeastern Brazil and the Sahel regions (Doi et al., 2009; Kushnir et al., 2006).

Transport of Saharan dust and other aerosols to the tropical North Atlantic: The Sahara is the largest source of atmospheric dust (Prospero et al., 2002; Yu et al., 2019), with our study area being one of the major regions impacted by it, as indicated by remote sensing data (Engelstaedter et al., 2006; Gläser et al., 2015; Ridley et al., 2012; Tanré et al., 2011). Besides the trade winds (Stuut et al., 2005; Swap et al., 1996), dust is also transported by the easterly mid-tropospheric Saharan Air Layer (Sarnthein et al., 1981), which prevails at altitudes between 1,500 and 6,000 m. The composition of desert dust includes key nutrients, with approximately 18 % Si, 4 % Ca, 4 % Fe, 0.8 ‰ P, 5‰ Mn of the dust mass, among other elements (Rodríguez et al., 2023, and references therein). These nutrients fuel primary productivity over vast distances (Bowie et al., 2001; Eglinton et al., 2002; Goudie and Middleton, 2001; Yu et al., 2015). Additionally, dust may influence climate by potentially inducing feedback processes (e.g., Cruz et al., 2021).

According to Mosquera Giménez et al. (2022) and the physico-chemical properties of the water types in the eastern North Atlantic (Liu and Tanhua, 2021), the water masses currently present in the region (Fig. 3; Supplementary Fig. S1) comprise: (1) surface waters, which include the mixed layer (0–50 m water depth) and the seasonal thermocline (50 m-150 m); (2) the South Atlantic Central Waters (~150 m-~500 m), which contain the permanent thermocline and are separated from the North Atlantic Central Waters by the Cabo Verde Frontal Zone (CVFZ). This CVFZ extends from Cape Blanc to the Cabo Verde islands (Pelegrí et al., 2017; Zenk et al., 1991) (Fig. 1a); (3) the Antarctic Intermediate Waters (~500 m-~1,200 m), which is generally considered to reach its northernmost limit at ~ 20°N (Talley, 2011; Liu and Tanhua, 2021); (4) North Atlantic Deep Water (~1,200 m-~3,500 m) (NADW). This water mass is a key component of the Atlantic Meridional Overturning Circulation (AMOC) and consists of three high-latitude water masses: Labrador Sea Water (LSW), Denmark Strait Overflow Water (DSOW) and Iceland-Scotland Overflow Water (ISOW) (Liu and Tanhua, 2021; Johns et al., 2021; Repschläger et al., 2021); (5) Northeast Atlantic Bottom Water (NEABW, 3,500–4,000 m, down to the seabed). A southern-sourced water mass derived from Antarctic Bottom Water (AABW), which is significantly modified during its northward

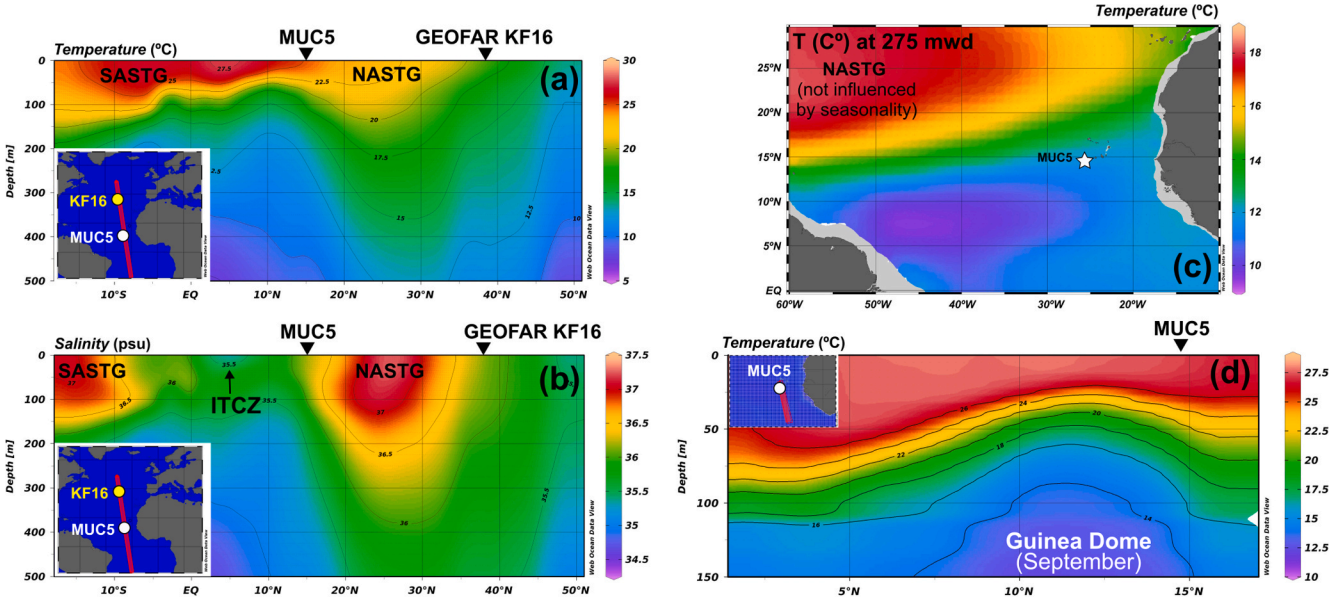

Fig. 2. North Atlantic Subtropical Gyre (NASTG) and Guinea Dome, the main oceanographic features influencing the study site. (a) Annual temperature N-S profile of the upper 500 m of the Atlantic Ocean. SASTG = South Atlantic Subtropical Gyre. (b) Annual salinity N-S profile of the upper 500 m. ITCZ = Intertropical Convergence Zone. (c) Annual temperatures at 275 m depth. The MUC5 sediment core location is marked by a white star. (d) September temperature profile of the upper 150 m in the Subtropical Northeast Atlantic. Maps and profiles sourced from Ocean Data View (Schlitzer and Mieruch-Schnülle, 2024) and World Ocean Atlas (WOA) (Reagan et al., 2024).

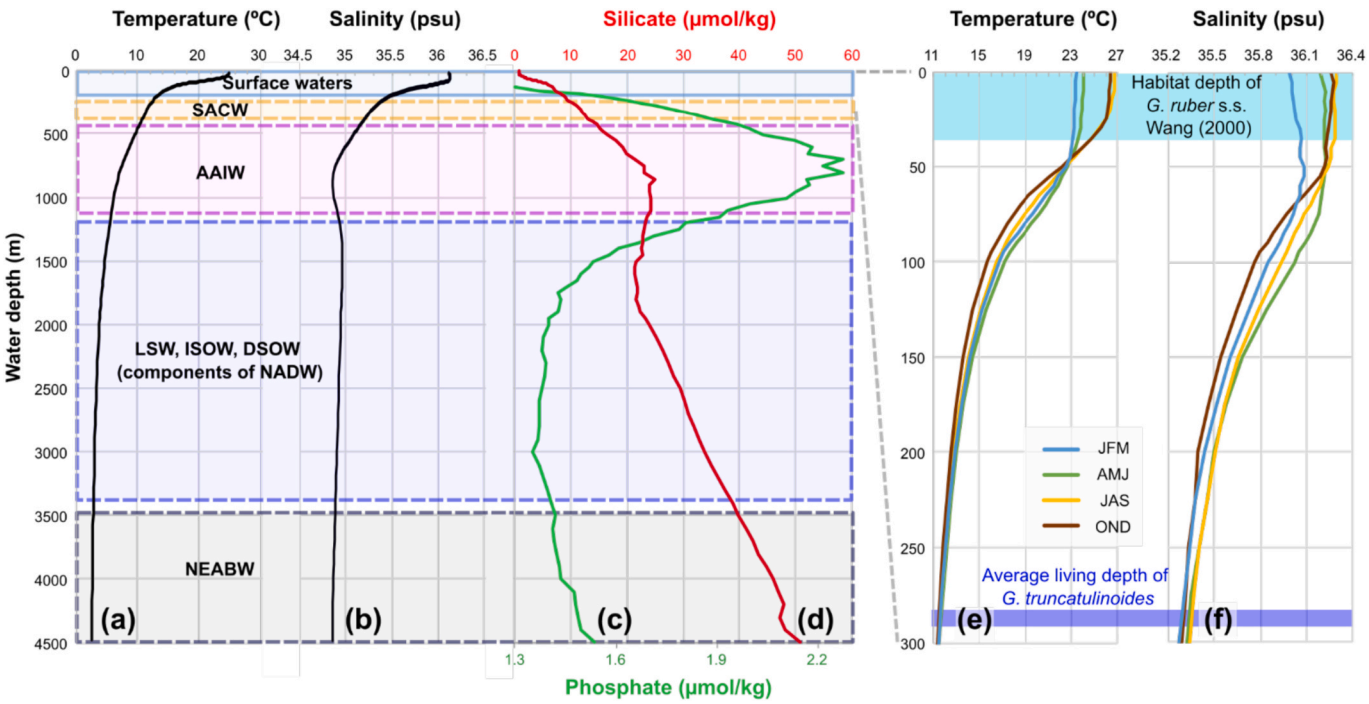

Fig. 3. Annual and seasonal oceanographic profiles from WOA station 426,572 (B), located at 14.625°N, 25.625°W (Reagan et al., 2024). Another station, 26287B, located at 14.5°N, 25.5°W, provides profiles of silicate and phosphate content. (a) Annual temperature of the upper 4,500 m. (b) Annual salinity of the upper 4,500 m. (c) Annual phosphate content of the upper 4,500 m. (d) Annual silicate content of the upper 4,500 m. Classification of water masses highlighted in a-d follow Mosquera Giménez et al. (2022) and Liu and Tanhua (2021): SACW = South Atlantic Central Waters; AAIW = Antarctic Intermediate Waters; LSW = Labrador Sea Water; ISOW = Iceland-Scotland Overflow Water; DSOW = Denmark Strait Overflow; NADW = North Atlantic Deep Water; NEABW = Northeast Atlantic Bottom Water. (e) Seasonal temperature of the upper 300 m. (f) Seasonal salinity of the upper 300 m. JFM = January-March (blue); AMJ = April-June (green); JAS = July-September (yellow); OND = October-December (brown). Shading marks (e) and (f) denote the habitat depth of *Globigerinoides ruber* s.s. according to Wang (2000) (light blue) and the assumed average living depth of *Globorotalia truncatulinoides* off East Africa, according to Steph et al. (2009) (dark blue).

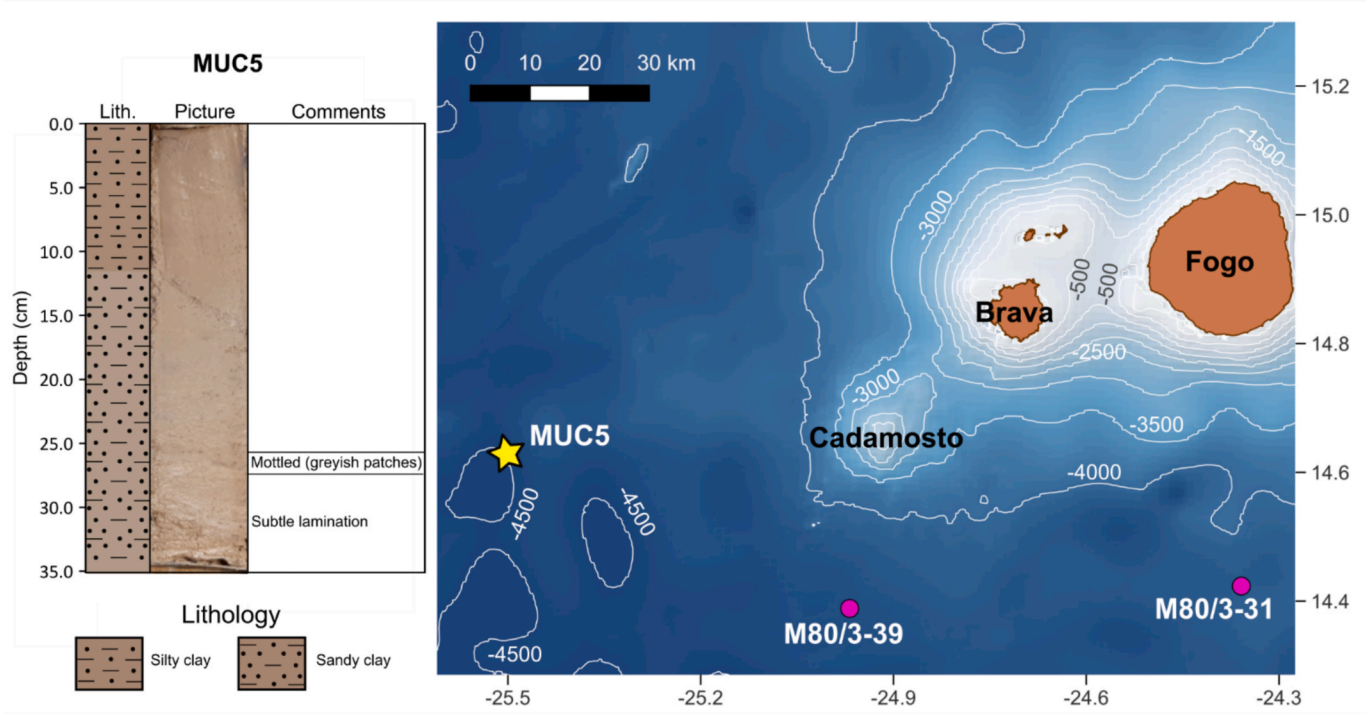

Fig. 4. Left: lithological description and core image of MUC5. Right: detailed location of core MUC5 in the southwest region of the Cabo Verde Archipelago. Cores indicated in pink were analysed by Eisele et al. (2015) and are referenced in this paper in relation with the tephra analyses. White lines represent the 500 m isobaths. The bathymetric map is sourced by the General Bathymetric Chart of the Oceans (GEBCO, 2021).

advection. NEABW is characterised by high silicate and phosphate content compared to NADW. According to Jenkins et al. (2015), bottom waters at the study site are composed primarily of ISOW and AABW in approximately equal proportions.

Geologically, the area is volcanically and seismically active due to the influence of an underlying mantle plume (Holm et al., 2006; Montelli et al., 2004; Pim et al., 2008). Volcanism began in the Oligocene, and since the Middle/Late Miocene this activity has resulted in the formation of the Cabo Verde Archipelago (e.g., Eisele et al., 2015; Ramalho, 2011). Fogo and Brava, the southwestern islands of the archipelago, along with the Cadamosto Seamount (located southwest of Brava) (Fig. 4), remain seismically very active (Grevemeyer et al., 2010; Madeira et al., 2010), with occasional explosive and effusive eruptions depositing lava and lapilli proximally, and ash distally in the surrounding sediments (e.g., Eisele et al., 2015). Similarly, the northwest island of Santo Antão, the submarine Charles Darwin Volcanic Field, and the Sodade Seamount are all characterized by high seismic activity (Kwasnitschka et al., 2024, and references therein).

Sedimentation ranges from hemipelagic to pelagic and includes sediments sourced from Saharan dust plumes, volcanic activity, and potential contributions from turbidites or landslides (deMenocal et al., 2000a, 2000b; Itambi et al., 2009; Jullien et al., 2007; Tisserand et al., 2009).

3. Materials and methods

3.1. Sampling and core descriptions

Core MUC5 (14.633°N, 25.501°W, 4,394 m water depth) was obtained from the abyssal plain, 84 km southwest of Brava Island (Fig. 1; Fig. 4) within the EU Horizon2020 project iAtlantic, during the iMirabilis2 expedition on board the R/V Sarmiento de Gamboa (UTM-CSIC) in 2021 (Orejas et al., 2022). It was retrieved by multicorer, and subsampled with a core liner of 7 cm diameter; coring methodology is available in Huvenne et al. (2022).

The lithology of MUC5 primarily comprises brownish-beige sandy to silty clay in the first 12 cm, transitioning to sandy clay, with the entire sandy fraction predominantly consisting of foraminiferal debris (Fig. 4). The core lacks both prominent sedimentary structures and interbedded siliciclastic-rich horizons. The sediments contain abundant bioclasts, principally foraminifera, along with rare to present occurrences of sponge spicules, and present to common radiolaria, as well as rare volcaniclastic fragments (glass shards or lava fragments) and minerals (quartz > pyroxene > plagioclase and amphibole ≫ foides and olivines).

3.2. Age-depth model

The AMS^{14}C dating was conducted at Beta Analytic, Inc. (Miami, US), using multi-species planktonic foraminifera picked from the > 125 μm fraction on a white tray to avoid selecting sediment-infilled specimens. A photograph of the dated sample is provided in Supplementary Fig. S2, illustrating the assemblage used. No local reservoir age correction was applied. The results were calibrated to years BP (before present) with a 95.4 % probability using the program BetaCal4.20 and the High-Probability Density Range Method, based on the MARINE20 calibration curve (Heaton et al., 2020). The "Conventional Radiocarbon Age" was determined using the Libby half-life (5.568 ka). The resulting ages were rounded to the nearest 10 years and the reported errors were based on 1σ counting statistics (Stuiver and Polach, 1977). When the calculated σ values were lower than 30 years BP on the Conventional Radiocarbon Age, they were rounded up to 30. Although 'ka' and 'kyr' are sometimes used to distinguish ages from durations (e.g., Aubry et al., 2009), we use 'ka' consistently for both throughout the manuscript for simplicity.

3.3. Electron microprobe analyses of tephras

In order to investigate the glass shard inventory of MUC5, we prepared smear slides of each sample in the 63–125 μm fraction. A total of twelve horizons appeared promising to contain at least some minerals and probable volcanic glass shards. This subset of samples was embedded for further electron microprobe (EMP) compositional analyses with the two-component epoxy resin araldite into 1-inch predrilled acrylic mounts having twelve 4 mm ø holes. Afterwards the sample surfaces were polished and subsequently the mounts were carbon-coated to provide discharge of the electrons during EMP measurements. However, only three of the twelve embedded samples contained glass shards. In total, 9 individual glass shards were analysed for major and minor elements using a JEOL JXA 8200 wavelength dispersive EMP at GEOMAR Helmholtz Center for Ocean Research Kiel, following the methods described in Kutterolf et al. (2011). A calibrated measuring program was used based on international standards with a 6nA sample current and 10 μm large electron beam to minimize sodium loss. Accuracy was monitored by two measurements each on Lipari obsidian (Lipari rhyolite; Hunt and Hill, 2001) and Smithsonian basaltic standard VGA99 (Makaopuhi Lava Lake, Hawaii; Jarosewich et al., 1980) before and after the sample measurements.

3.4. X-ray fluorescence (XRF) scans

X-ray fluorescence (XRF) scanning of the MUC5 sedimentary sequence was performed at the Institute of Geosciences, Christian-Albrechts-University, Kiel, Germany, utilizing an Avaatech XRF core scanner. To avoid sample surface contamination, the split core was covered with a thin mylar film before being mounted in the XRF scanner. Data acquisition was carried out at 0.5 cm spatial resolution, using tube voltages set at 10 kV for relatively lighter elements, and 30 kV for heavier elements, with tube currents of 200 μA and 1,000 μA, respectively. This non-destructive technique yields high-resolution continuous elemental data, useful for understanding various palaeoenvironmental processes (Arz et al., 1998; Croudace and Rothwell, 2015). However, the results are semi-quantitative due to their dependence on sediment physical properties such as grain size, density, or water content. To minimize this effect, several elemental ratios were calculated instead of using individual elements. Furthermore, following the approach recommended by Weltje and Tjallingii (2008), natural logarithms (ln) of these ratios were used to ensure statistically valid comparisons.

The following ln-ratios were employed as proxies:

1) Fe/K, which typically shows higher values in fluvial sediments compared to aeolian sediments (Mulitza et al., 2008; Stuut et al., 2005; Govin et al., 2012). Consequently, increases in the Fe/K ratio are interpreted as indicative of more humid conditions (e.g., Zarriess and Mackensen, 2010).

2) Zr/Rb, which serves as a proxy for grain size (Croudace and Rothwell, 2015), may therefore indicate changes in sediment provenance and/or transport dynamics. This relationship between grain size and this elemental ratio occurs because Zr is predominantly hosted in silt-sized zircons. Zircons are heavy minerals that sort with sand-size siliciclastic fractions due to their higher density (Lamy et al., 2015), whereas Rb indicates increased clay contribution to the sediments (Rothwell et al., 2006), because it is mainly found substituting K in clay minerals from felsic sources (Schneider et al., 1997). Some studies have also linked Zr/Rb to near-bottom current velocities (Gauchery et al., 2021; Mirzaloo et al., 2019; Wu et al., 2020); however, in this case, the sluggish nature of deep bottom waters (e.g., Bourlès et al., 2003) makes it uncertain whether hydrodynamic sorting significantly affects the size distribution of bottom sediments.

3) Ca/Ti, which reflects the carbonate biogenic production (Croudace and Rothwell, 2015) *vs* the terrigenous input. Carbonates in this context primarily originate from nannoflora and planktonic foraminifera dwelling in the euphotic zone, sinking through the water

column upon death. On the other hand, Ti is exclusively of detrital origin and nonreactive during early diagenetic processes (Gottschalk et al., 2018); therefore, it is related to the quantity of lithogenic input.

3.5. Planktonic foraminifera assemblages and other micropalaeontological proxies

Analyses were performed at every centimetre throughout MUC5, comprising a total of 35 samples. Core samples were weighted before and after being oven-dried at 40 °C to determine their water content. Subsequently, samples were washed with distilled water and split into two fractions (63–125 μm, and > 125 μm) using sieves that had been cleaned in an ultrasonic bath to prevent contamination. Planktonic taxa were counted on a sample split with a minimum population of 300 individuals from a dry-sieved > 150 μm fraction at the Centro Oceanográfico de Vigo, Instituto Español de Oceanografía, IEO-CSIC (Spain). The species found in MUC5 were classified according to the taxonomic review of Brummer and Kučera (2022), with the following exceptions: (1) *Globigerinita uvula* and *Globigerinita minuta* were combined into one category; (2) *Globigerinella calida* and *Globigerinella radians* were also not differentiated and were counted in a single category; (3) the name *Globorotalia menardii* was selected over *Globorotalia cultrata*, the proposed valid name according to Brummer and Kučera (2022). This decision is based on the widespread use and recognition of *G. menardii* for Miocene and younger menardii-form species (Stainforth et al., 1975). The following categories were also created to include unidentified specimens: *Globorotalia* spp., *Globorotalia* juvenile and *Globigerinoides* spp. Moreover, the number of benthic foraminifera and radiolaria was simultaneously logged in each sample.

In addition to relative abundance of planktonic species, several palaeoecological proxies were calculated, including: (1) accumulation rate of planktonic foraminifera and radiolaria, which reflects marine bioproductivity at the sea surface. This parameter is calculated using the following equation described in O'Brien et al. (2021):

$$\text{Accumulation rate} = \#/g \times \rho \times \textit{sedimentation rate} \quad (1)$$

Here, #/g represents the number per wet gram of sediment, and ρ denotes the density of the wet sediment, derived from the dry mass and mass of water. An average grain density of 2.65 g/cm^3, and a water density of 1.027 g/cm^3 are assumed for this calculation. (2) The Simpson Biodiversity Index, which is a measure to assess assemblage diversity by considering both the number of species present and their relative abundance. It was calculated with the following formula:

$$S = 1-\sum_i \left(\frac{n_i}{n}\right)^2 \quad (2)$$

Where n is the total number of individuals and n_i is the number of individuals of each taxon i. This index ranges from 1 to 0, where higher values indicate greater diversity and lower dominance, while lower values signify the opposite. (3) The relative abundance (%) of species with a preference for upwelling conditions (*Globigerina bulloides*, *Globorotalia inflata*, and *Neogloboquadrina incompta*) (Meggers et al., 2002; Thiede, 1975), along with those inhabiting warm biogeographic water domains (Brummer and Kučera, 2022). (4) Planktonic foraminifera fragmentation percentages used as a dissolution index, which is the number of shell fragments divided by the sum of fragments and entire shells.

We refrain from calculating transfer functions based on planktonic foraminiferal assemblages because of problems encountered with temperature estimation using this method at the nearby ODP site 658C (Adkins et al., 2006). These issues are probably due to the fact that planktonic foraminiferal assemblages at low latitudes are more influenced by the structure of the upper ocean layers (Telford et al., 2013), which at this site is shaped by seasonal upwelling, rather than by water temperature (Wolff et al., 1999, and references therein).

3.6. Geochemistry of the foraminifera shells

Combined Mg/Ca and stable carbon and oxygen isotope ($\delta^{13}C$ and $\delta^{18}O$) analyses were performed at GEOMAR, Helmholtz-Centre for Ocean Research, Kiel (Germany), on foraminifera shells extracted from samples collected at 1 cm intervals along core MUC5. Approximately 45 specimens each of the surface-dwelling planktonic foraminifera *Globigerinoides ruber albus* (following the concept of *G. ruber* s.s. of Wang, 2000), and the sub-thermocline dwelling *Globorotalia truncatulinoides*, were selected from sieved sediment samples of the 315–400 μm fraction, in order to minimize size-related effects on either Mg/Ca or stable isotopes. Additionally, $\delta^{13}C$ and $\delta^{18}O$ measurements were conducted on an average of ~ 3 specimens of the epibenthic foraminifera *C. wuellerstorfi*. Fig. 3 and Supplementary Text S1 provide more information on the habitat of the three species selected for geochemical analysis.

3.6.1. Carbon and oxygen ($\delta^{13}C$ and $\delta^{18}O$) stable isotopes

Stable isotopes were analysed on a Thermo Scientific MAT 253 mass spectrometer equipped with an automated Kiel IV carbonate preparation device. Isotope values were calibrated against the NBS 19 (National Bureau of Standards) carbonate standard and the in-house carbonate standard "Standard Bremen" (Solnhofen limestone). Isotope values are reported in the δ notation relative to the Vienna Pee Dee Belemnite (VPDB) standard in per mil. Refer to Supplementary Fig. S3 for downcore stable carbon and oxygen isotopic results of *G. ruber* s.s. (Wang, 2000) and *G. truncatulinoides*, and to Supplementary Fig. S4 for the isotopic signature of *G. truncatulinoides* with respect to its encrustation stage. Carbon isotope values are interpreted in terms of bioproductivity and nutrient inventory, and also provide insights into the prevailing water mass. Oxygen isotope values are dependent on global ice volume, regional water temperature and salinity.

3.6.2. Mg/Ca palaeo-thermometry

The samples underwent the cleaning procedures outlined by Boyle and Keigwin (1985) and Boyle and Rosenthal (1996) before the geochemical analyses, which include oxidative and reductive cleaning steps. Mg/Ca analyses were performed using a Varian 720 ES axial-viewing ICP-OES (Inductively Coupled Plasma Optical Emission Spectrometry), with detection levels typically ranging from 0.001 to 0.1 μg/ml. Mg/Ca results were normalized to the ECRM 752–1 standard (3.761 mmol/mol Mg/Ca) and drift-corrected. Regular analyses of the ECRM 752–1 standard yielded an analytical error of ± 0.01 mmol/mol for Mg/Ca.

In terms of the impact of dissolution on foraminiferal Mg/Ca, the effects are primarily influenced by the calcite saturation state of the bottom waters. Regenberg et al. (2014) defined a global critical threshold for dissolution of 21.3 ± 6.6 μmol/kg $\Delta[CO_3^{2-}]$. At our studied site, this threshold is reached at a depth of ~ 2,700 m (Regenberg et al., 2014). Since MUC5 was collected from ~ 4,400 m water depth, calcite dissolution may have affected the foraminiferal Mg/Ca to some extent. Nonetheless, while the results should be interpreted with a degree of caution, there is supporting evidence for the reliability of our temperature estimates, which are discussed in Supplementary Text S1 and Supplementary Fig. S5.

In addition, simultaneous measurements of Al, Fe and Mn were conducted to monitor the potential presence of aluminosilicates that can contaminate the tests, altering the Mg/Ca signal. These indicators do not suggest major contamination. The results and discussion of these measurements can be found in Supplementary Text S1 and Supplementary Figs. S6 and S7.

Globigerinoides ruber s.s. (Wang, 2000) Mg/Ca ratios (Mg/Ca_{ruber}) were converted to $SST_{Mg/Ca}$ using the following species-specific temperature calibration for the Atlantic (Dekens et al., 2002):

$$Mg/Ca = 0.38 \times \exp(0.09[SST-0.61\ (\text{core depth km})]) \quad (3).$$

This calibration was chosen from a range of equations because it was derived from Atlantic material and it provides more realistic results for this site (Supplementary Fig. S8 and Supplementary Text S1). Overall, our reconstructed SSTs showed good agreement with modern data (WOA23; Reagan et al., 2024), however, one data point, exhibiting an anomalously high Mg/Ca value, not supported by a corresponding $\delta^{18}O$ anomaly, was excluded from subsequent analyses (Supplementary Fig. S6 and Supplementary Text S1). Given the preference of *G. ruber albus* for warm, oligotrophic waters, the $SST_{Mg/Ca}$ estimations may be slightly biased toward the non-upwelling season (c.f. Supplementary Text S1).

Globorotalia truncatulinoides Mg/Ca ratios ($Mg/Ca_{truncatulinoides}$) were converted to $subSST_{Mg/Ca}$ using the following species-specific temperature calibration (Cléroux et al., 2008):

$$Mg/Ca = 0.62 \times \exp(0.074 subSST) \quad (4)$$

This calibration was chosen over others because it yields more realistic values for this site (Supplementary Fig. S8 and Supplementary Text S1). Our derived subSST estimates also show good agreement with modern hydrographic data.

Removing the influences of global ice volume and temperature from the $\delta^{18}O$ signal enables the derivation of $\delta^{18}O$ of seawater ($\delta^{18}O_{sw}$), which approximates palaeosalinity (e.g., Nürnberg et al., 2008). The temperature effect was subtracted from the initial foraminiferal $\delta^{18}O$ by using the Bemis et al. (1998) equation for planktonic foraminifera: $\delta^{18}O_{sw} = 0.27+((T\text{-}16.5 + 4.8 \times \delta^{18}O_{foram})/4.8)$. By adding 0.27 ‰ to the formula, we convert the calcite on the VPDB standard values, to water on the Vienna Standard Mean Ocean Water (SMOW) (Hut, 1987). We used the relative sea level reconstruction of de Boer et al. (2014) to eliminate the effect of global ice volume variability from the $\delta^{18}O_{sw}$ data, leading to regional ice-volume-corrected values ($\delta^{18}O_{sw\text{-}ivc}$).

In this study, sea surface $\delta^{18}O_{sw\text{-}ivc}$ is calculated from $\delta^{18}O_{ruber}$ and the according $SST_{Mg/Ca}$. Sub-thermocline $\delta^{18}O_{sw\text{-}ivc}$ is determined from the $\delta^{18}O_{truncatulinoides}$ and $subSST_{Mg/Ca}$. Lower $\delta^{18}O_{sw\text{-}ivc}$ values imply fresher conditions. We did not convert the results to practical salinity units (psu) due to potential inaccuracies associated with this type of reconstruction at low latitudes (Holloway et al., 2016; Schmidt, 1999). However, $\delta^{18}O_{sw\text{-}ivc}$ results reconstructed from *G. ruber* s.s. (Wang, 2000) and *G. truncatulinoides* from the core-top align reasonably well with modern seawater $\delta^{18}O$ values, which are ~ 0.5–1 ‰SMOW for surface waters and ~ 0.4–0.8 ‰SMOW at water depths of 200–300 m (Schmidt et al., 1999).

4. Results

4.1. Age-depth model

The core chronology for MUC5 is based on a second-degree polynomial regression fit through three Accelerator Mass Spectrometry (AMS) radiocarbon (^{14}C) dates on mixed planktic foraminifera (Table 1; Fig. 5).

These analyses indicate that the sedimentary sequence of MUC5 extends from ~ 11.2 ka BP to ~ 1.3 ka BP, covering most of the Holocene period. The non-modern core-top age (1.3 ka BP) is not attributed to the absence of modern sediments, as the core-top revealed an undisturbed surface layer with no signs of erosion (Fig. 4; Huvenne et al., 2022). Relatively older age core-tops are a common feature in deep-sea cores dated using ^{14}C (Broecker et al., 1991; Mekik, 2014) likely due to bioturbation effects in cores with low sedimentation rates (Manighetti et al., 1995).

Table 1
Radiocarbon dates (AMS^{14}C) used for the sediment core MUC5 age model.

Sample depth (cm)	Beta ID	Conventional radiocarbon age (ka BP)	Calibrated radiocarbon age (ka BP)	Mean calibrated radiocarbon age (ka BP)
0–1	Beta - 635553	1.870 ± 0.03	1.388–1.127	1.257 ± 0.130
21–22	Beta - 635554	6.220 ± 0.03	6.615–6.300	6.457 ± 0.157
33–34	Beta - 635555	9.910 ± 0.04	11.005–10.548	10.776 ± 0.228

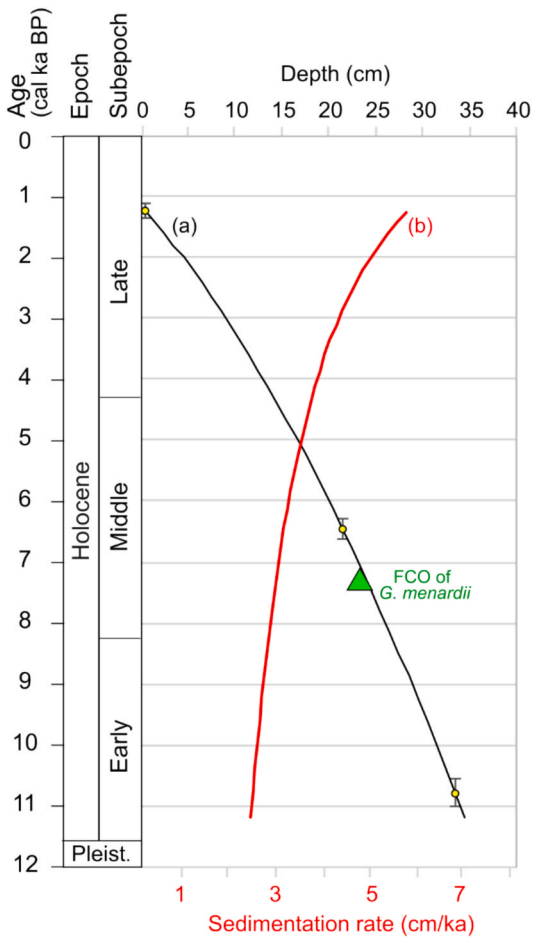

Fig. 5. (a) Depth/age relationship of the sediment core MUC5: yellow dots = age control points (AMS radiocarbon age), black line = second-degree polynomial regression; vertical bars = 1σ error. (b) Sedimentation rate. Green triangle = First common occurrence (FCO) of *Globorotalia menardii* occurring at 23.5 cm depth in MUC5 and dated as ~ 7.5 ka BP by Broecker and Pena (2014).

The reliability of the MUC5 age model is supported by the timing of the first common occurrence (FCO) of *G. menardii*. According to our age-depth model, this occurs between 7.4 ka BP and 7.1 ka BP in MUC5, consistent with the age of ~ 7.5 ka BP reported for the reappearance of *G. menardii* in mid-latitudes regions of the Atlantic Ocean, after its absence during the last glacial period (Broecker and Pena, 2014, and references therein) (Fig. 5).

The inferred sedimentation rate shows a decreasing trend throughout MUC5, with a maximum value of ~ 6 cm/ka observed at the top of the core and a minimum value of ~ 2 cm/ka at the base (Fig. 5b). The average rate of ~ 4 cm/ka fits reasonably well into the regional setting, being lower than the estimated sedimentation rate of 18 cm/ka at the proximal ODP Site 658C (deMenocal et al., 2000a) (Fig. 1a), but higher than the rate of ~ 2 cm/ka estimated by Broecker et al. (1991) for the INMD101 core location, situated at a similar longitude but closer to the equator (Fig. 1a).

4.2. Sediment supply: Tephra input and lithogenic vs carbonate contributions from XRF and microfossil accumulation data

The results of the tephra analyses show that the overall abundance of volcanic glass is rare and dispersed within the background sediment. Only three intervals contained fresh volcanic glass for further geochemical analyses. These samples are all located in the upper half of the core at 5–6 cm (2.2 ka BP), 9–10 cm (3.1 ka BP), and 15–16 cm depth (4.7 ka BP). All nine analysed glass shards are phonotrephitic to tephrophonolitic (Supplementary Table S1; Fig. 6).

To further investigate changes in sediment supply, we evaluated XRF data (in which Ca is the most abundant element, with other common elements including Fe, Si, Ti, and K) and planktonic foraminiferal accumulation rates as complementary environmental proxies (see Sections 3.4 and 3.5). The key results are summarized below:

1) ln Fe/K show the lowest values from the core base up to ~ 10 ka BP. The numbers remain generally high between ~ 10 and ~ 5.5 ka BP, with a maximum between ~ 6 and ~ 7 ka BP, and decrease thereafter, although a minor anomaly of low values is observed around 2 ka BP (Fig. 7a).

2) ln Zr/Rb shows low values until ~ 7.5 ka BP, followed by a period of elevated values between ~ 7.5 and ~ 5.5 ka BP. After this interval, values gradually decrease and stabilize at lower levels from ~ 4 ka BP onward (Fig. 7b).

3) ln Ca/Ti ratios are relatively high from the base of the core to ~ 10.5 ka BP, then decrease and remain low between ~ 10.5 and ~ 7.5 ka BP. From ~ 7.5 ka BP onwards, Ca/Ti values rise to intermediate levels and exhibit a slight overall decreasing trend (Fig. 7c).

4) The average planktonic foraminiferal accumulation rate is ~ 24,400 #/cm^2/ka. Values are relatively high between the base of the core and ~ 10 ka BP, then decrease and remain low between ~ 10 and ~ 8 ka BP, with a minimum of ~ 7,500 #/cm^2/ka recorded at 9.6 ka BP. Between ~ 8 and ~ 5 ka BP, accumulation rates return to intermediate levels, followed by the maximum value at 4.7 ka BP, reaching ~ 37,100 #/cm^2/ka. After this peak, values decrease again to intermediate levels (Fig. 7d).

Fig. 7e-h present additional regional proxies that help contextualize the lithogenic input changes observed in the study area.

4.3. Microfossil assemblages

A total of 35 species of planktonic foraminifera were identified in core MUC5. On average, each sample contained 26 species. Dominant species include *G. ruber albus* (averaging 18.5 %), *N. incompta* (14 %) and *Trilobatus sacculifer* (12 %). Species with average abundances ranging from 10 % to 5 % comprised *Globigerinita glutinata*, *G. bulloides*, *Globigerinoides ruber ruber*, *G. menardii* and *G. inflata*. The remaining species contributed less than 5 % on average each to the total. Fig. 8a-f shows the relative abundances of planktonic foraminiferal species undergoing prominent changes in MUC5, while Fig. 8g presents the Simpson biodiversity index. The highest rate of change is recorded between ~ 8 and ~ 7 ka BP, coinciding with a notable increase in biodiversity. Reflecting this faunal turnover, *G. inflata*, *G. bulloides*, and *N. incompta* decrease markedly, whereas *G. menardii*, *T. sacculifer* and *G. ruber albus* show a gradual increase throughout the Holocene. Supplementary Table S2 provides a more detailed description of the faunal turnover outlined here and the preferred habitats of these species.

Additionally, two relatively short-lived events affecting individual samples were observed: 1) At 4.7 ka BP, a radiolaria bloom was recorded, with an accumulation rate exceeding ~ 20,000 #/cm^2/year (Fig. 8h), compared to the core average of ~ 1,100 #/cm^2/year. This event was accompanied by slight increases in the percentages of *G. bulloides* (Fig. 8b) and *N. incompta* (Fig. 8c), along with the highest planktonic foraminifera accumulation rate recorded within our dataset (Fig. 7d). 2) At 2.9 ka BP, a notable increase in *G. ruber albus* was observed, reaching 35.8 % relative abundance compared to the core average of 18.6 % (Fig. 8f). This led to a brief but significant decline in the biodiversity curve (Fig. 8g).

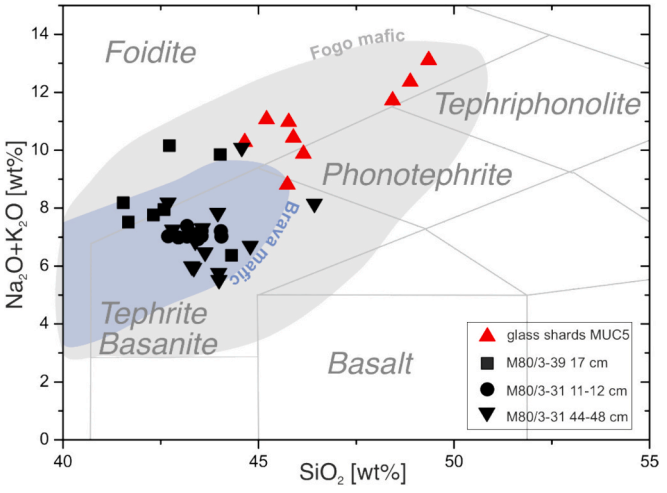

Fig. 6. Total alkalis *vs* silica classification diagram (Le Maitre et al., 2002). Single glass shard analyses for MUC5 are plotted together with comparison data for three layers from the respective time interval reported in Eisele et al. (2015) and compositional fields for Fogo and Brava mafic compositions (modified after Eisele et al., 2015, and references therein).

4.4. Geochemical proxies from planktonic foraminifera

The average $SST_{Mg/Ca}$ is 26 °C, with a range of 2 °C between the highest and lowest recorded values (Fig. 8i). The warmest temperatures are observed during the Middle Holocene.

The average $subSST_{Mg/Ca}$ is 12 °C, with a range of 2 °C between the highest and lowest recorded values (Fig. 8j). Additionally, three distinct cooler intervals are identified, each reflecting an approximate 3 °C drop. These intervals correspond to the Early Holocene and two periods in the Late Holocene (~3.4–2.7 ka BP and ~ 2.0–1.3 ka BP).

The reconstructions of the surface and subsurface $\delta^{18}O_{sw\text{-}ivc}$ show a relatively high degree of variability (Fig. 8k-l). Overall trends suggest that the salinity gradient diminished during the Middle Holocene, primarily due to slightly elevated subsurface values (despite some fluctuations) and a decrease in surface values around 6–7 ka BP.

Additionally, isotopic values show, in broad terms, a slight increasing trend in $\delta^{13}C$ during the Early and Middle Holocene in both *G. ruber* s.s. (Wang, 2000) and *G. truncatulinoides*, followed by fluctuating values without a clear trend in the Late Holocene. $\delta^{18}O$ values in both species show a slight decreasing trend during the Early and Middle Holocene. During the Late Holocene, *G. truncatulinoides* $\delta^{18}O$ records vary without a clear trend, whereas *G. ruber* s.s. values show an increased trend, except in the uppermost samples, where they decrease again (Supplementary Fig. S3).

Fig. 9 illustrates additional data relevant to the evolution of palaeoceanographic proxies in MUC5, providing broader context for interpreting the influence of NW African upwelling during the Holocene at the study site. SST from MUC5 is shown in Fig. 9a, along with the relative abundance of *G. ruber ruber* (Fig. 9b), the species with the highest affinity for warm surface waters. Fig. 9c-h present SST and productivity-related records from other regional sites.

4.5. Palaeoceanographic indicators of bottom waters conditions

Stable carbon and oxygen isotopes from *C. wuellerstorfi* (Fig. 10a-b), along with planktonic foraminifera fragmentation rates (Fig. 10c), were measured in core MUC5 to investigate changes in bottom water geochemistry in the northeastern subtropical Atlantic throughout the Holocene.

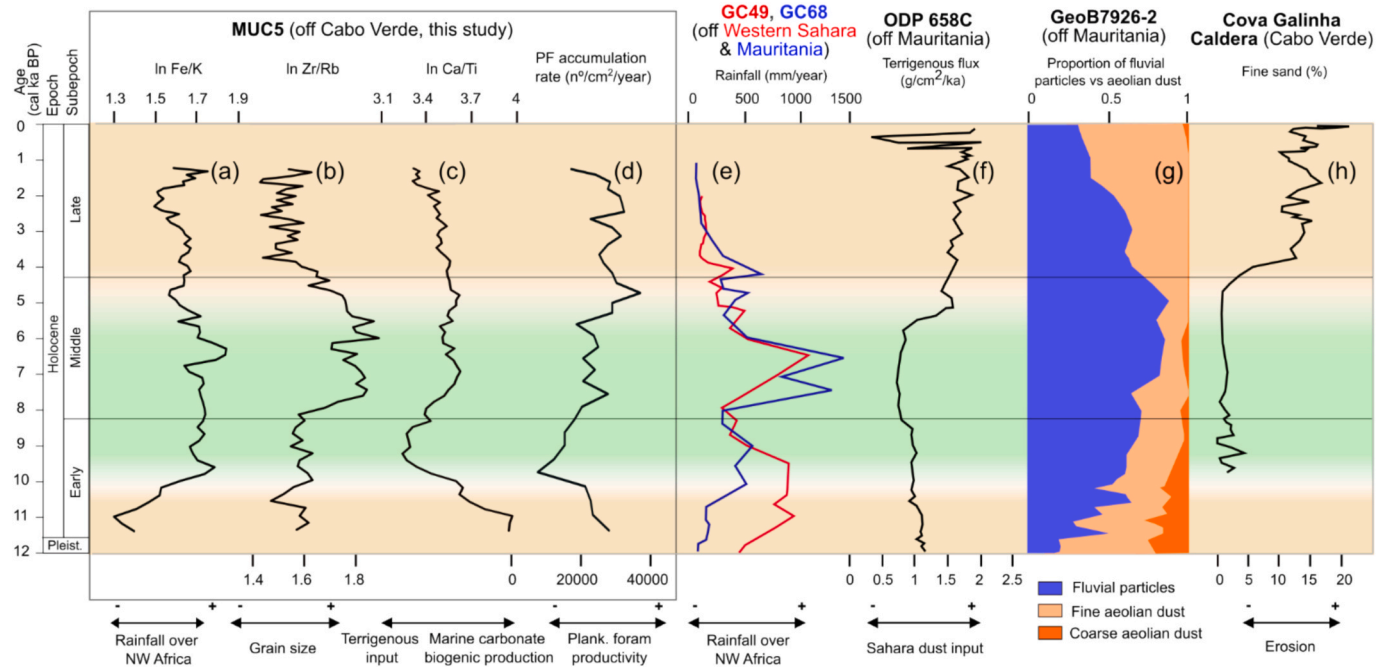

Fig. 7. XRF-based elemental ratios and planktonic foraminifera accumulation rate of core MUC5 compared to other proxy records from the region. (a-c) XRF ln ratios of core MUC5. (d) Planktonic foraminifera accumulation rate of core MUC5. (e) Rainfall estimation from cores GC49 and GC68 (Tierney et al., 2017). (f) Terrigenous flux of Site 658C (Adkins et al., 2006; deMenocal et al., 2000a). (g) Contribution of fluvial particles compared to fine and coarse aeolian dust (McKay et al., 2014). (h) Relative abundance of fine sand at Cova Galinha Caldera (Brava Island, Cabo Verde; Castilla-Beltrán et al., 2021). Brown shading = drier climate and the development of a desert in the Sahara; green shading = wetter climate of the AHP.

$\delta^{13}C$ records from *C. wuellerstorfi* show a general increasing trend throughout the Holocene. During the Early Holocene, values are relatively low, ranging between 0.06 and 0.7 ‰ VPDB. In the Middle Holocene, values are generally higher, exceeding 0.7 ‰ VPDB in most samples, although a sharp drop is observed at 6.8 ka BP, reaching approximately − 0.07 ‰ VPDB. At the onset of the Late Holocene, $\delta^{13}C$ values decrease again, followed by a broad increasing trend through the remainder of the period (Fig. 10a). $\delta^{18}O$ values from *C. wuellerstorfi* are relatively heavy during the Early Holocene. In the Middle Holocene, values are intermediate, mostly ranging from 2.5 to 2.9 ‰ VPDB, with a marked peak at 6.8 ka BP reaching 3.9 ‰ VPDB. At the onset of the Late Holocene, $\delta^{18}O$ values increase again slightly, followed by relatively low values throughout the remainder of the Late Holocene (Fig. 10b).

Planktonic foraminifera fragmentation shows values of ~ 25 % during the Early Holocene, relatively lower values during the Middle Holocene (~15–20 %), with a brief increase around 5–6 ka BP, and the highest values of the record occurring during the Late Holocene (~30–40 %) (Fig. 10c).

To contextualise bottom water geochemistry at the study site, we compare our data with benthic foraminiferal $\delta^{13}C$ records from the Azores (Repschläger et al., 2015; Fig. 10d) and south of Iceland (Thornalley et al., 2010; Fig. 10e). Fig. 10f shows the sortable silt record from Thornalley et al. (2013), stacked from several high-latitude sites and interpreted by the authors as a proxy for ISOW strength; sortable silt refers to the mean grain size of the 10–63 μm terrigenous fraction, which reflects changes in bottom current velocity (McCave et al., 2017).

5. Discussion

5.1. Sediment composition and its link to marine and continental environmental variability

In this subsection, we discuss the sediment contributions to the site based on tephra shard identification, lithogenic input inferred from XRF data and core descriptions, and marine carbonate production from XRF-derived Ca content and planktonic foraminifera accumulation rates.

The analysis of tephra contents led to the recovery and identification of nine glass shards in MUC5. Their compositions are phonotrephitic to tephrophonolitic (Supplementary Table S1) and comparable to compositions known from Fogo and Brava eruptions, as described by Eisele et al. (2015) (Fig. 6). That study also described three widespread mafic tephra layers within the last 6 ka, which they tentatively correlated to a Fogo source. The geochemical compositions of these layers (M80/3–31, 11–13 cm; M80/3–31, 44–48 cm; and M80/3–39, 17–18 cm) do not correlate with any of the glass shard compositions measured in MUC5 (Fig. 6). However, the MUC5 glass shards fall within the compositional fields for volcanics known from Fogo and Brava, thus pointing to these islands as a potential source.

The scarcity of glass shards at the site suggests limited influence from explosive volcanic activity in the Cabo Verde region on local sedimentation during the Holocene.

As shown by the XRF data, Ca predominates in MUC5, reflecting the importance of marine calcareous biogenic production as a main source of material reaching the seafloor. Variations in this production may be influenced by nutrient input from Saharan dust and/or by changes in the regional upwelling system. Although this site lies in a relatively oligotrophic setting, a modest intensification of upwelling may have favoured calcareous plankton such as coccolithophores and foraminifera, which typically do not thrive under intense upwelling conditions. Other common elements (e.g., Fe, Si, Ti, K) are likely related to lithogenic input and, in the absence of significant volcanic eruptions, presumably reflect variations in sediment sources and/or environmental changes in Northwest Africa.

The sediment compositional variations inferred throughout MUC5 (Fig. 7) are associated with the following distinct environmental intervals:

Preboreal, from the base of the core at 11.2 ka BP until ~ 10 ka BP: The low Fe/K ratios (Fig. 7a) observed at the base of the core are indicative of the Preboreal period, characterised by arid conditions in Northwest Africa (e.g., deMenocal et al., 2000a).

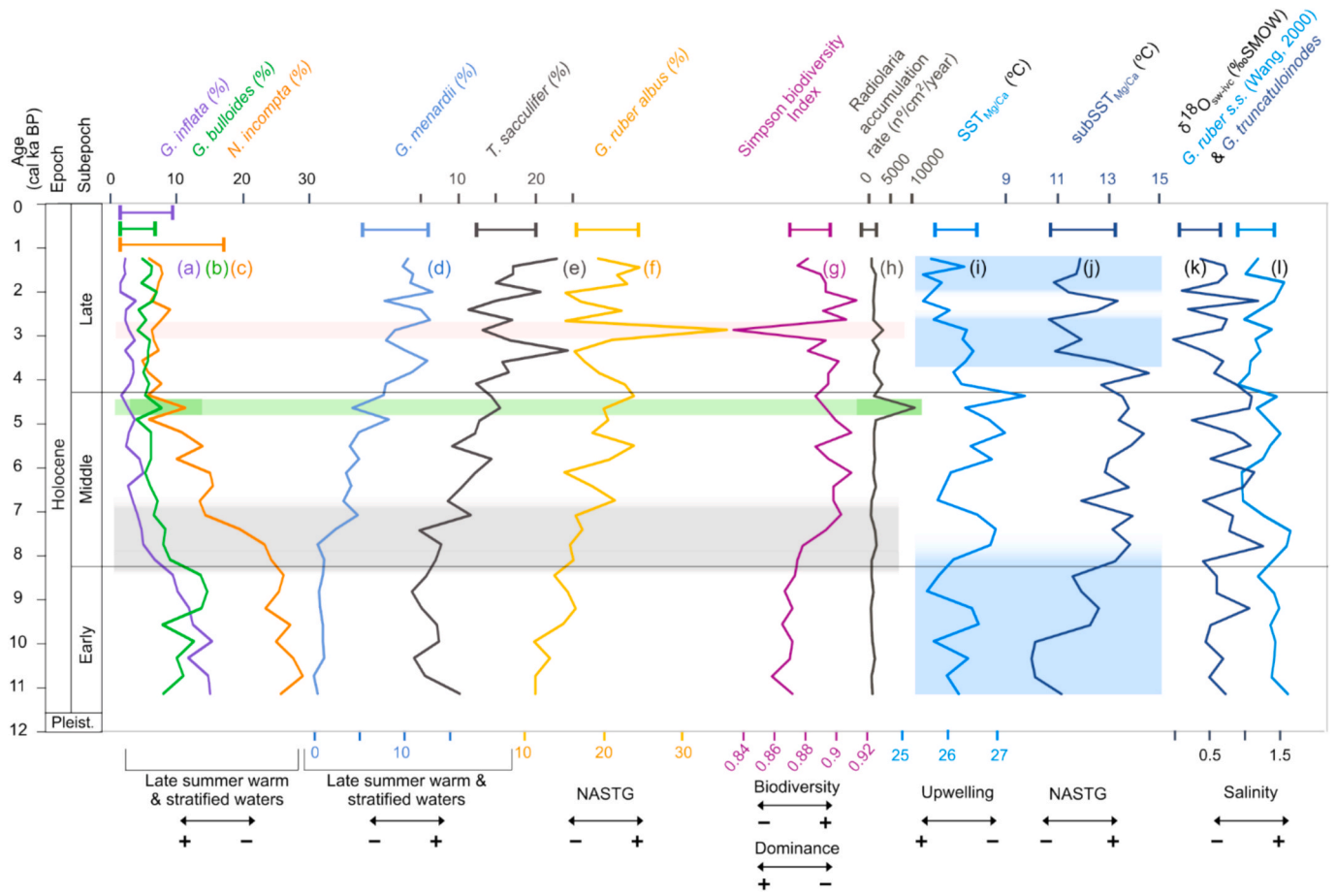

Fig. 8. Holocene proxy variability recorded in core MUC5. (a-f) Relative abundances of planktonic foraminiferal species undergoing prominent changes during the Holocene. (g) Simpson biodiversity index. Grey shading = interval marked by increased turnover in planktonic foraminiferal assemblages, with simultaneous rise in biodiversity. Green shading = sample indicating enhanced productivity. Pink shading = sample of increased abundance of *G. ruber albus*, associated with reduced biodiversity. (h) Radiolaria accumulation rate, note the brief but important increase at 4.7 ka BP highlighted in green. (i) $SST_{Mg/Ca}$. (j) $subSST_{Mg/Ca}$. Blue shading = periods of sea surface and subsurface cooling. Sea surface (k) and subsurface $\delta^{18}O_{sw\text{-}ivc}$ (approximation for salinity) (l). Horizontal bars = 2σ error.

Zr/Rb values are relatively low (Fig. 7b), indicating comparatively fine grain sizes. This may reflect aridity over the continent, which could have led to enhanced deposition of fine-grained aeolian material from the Sahara. Such sediments have high clay contents (Rodríguez-Navarro et al., 2018) and are therefore likely relatively enriched in Rb. This is consistent with findings from GeoB7926-2 off Mauritania (McKay et al., 2014), where a predominance of aeolian dust is observed during this period (Fig. 7g), but not at the nearby Site 658C (Adkins et al., 2006; deMenocal et al., 2000a), where terrigenous input appears to be minimal (Fig. 7f). However, a change in grain size is not evident from the visual inspection of MUC5 (Fig. 4). Thus, the interpretation of low Zr/Rb values as indicative of finer grain sizes during the Preboreal Period remains tentative, and would benefit from complementary sedimentological analyses.

The elevated Ca/Ti ratios (Fig. 7c), and the planktonic foraminifera accumulation rates (Fig. 7d) suggest increased biogenic carbonate production, possibly driven by fertilisation of the upper ocean layers through enhanced Sahara dust input, resulting from continental aridity and/or oceanographic conditions more favourable to carbonate producers. It is noteworthy that the humidity proxy (Fe/K) exhibits an overall trend opposite to that of marine carbonate production indicators (Ca/Ti and planktonic foraminiferal accumulation rate), suggesting that humid phases were less favourable for carbonate accumulation. This may result from the direct impact of increased rainfall on the physical and chemical properties of the upper ocean layers. Additionally, the same climatic conditions that enhance the West African Monsoon could reduce foraminiferal productivity by altering upwelling dynamics and/or the influence of the Guinea Dome in the subtropical eastern Atlantic. Another contributing factor to this opposite trend could be the increased input of terrigenous material, which may dilute the concentration of marine biogenic carbonates.

The AHP, from ~ 10 ka BP to ~ 5.5 ka BP: This interval is characterised by high Fe/K ratios (Fig. 7a), which persist until ~ 6 to 5.5 ka BP, indicative of increased African river discharge and reduced dust input. The fluvial sediment transportation to the site, which is relatively distant from the North African coast, might have been facilitated by the well-developed regional fluvial network at the time (Skonieczny et al., 2015). Additionally, offshore advection of particles can be driven by vigorous turbulent mixing resulting from the confluence of various water masses off Cape Blanc and regional upwelling, which effectively resuspends shallow shelf sediments and transports particles offshore, as seen in present day studies (Gabric et al., 1993; Karakaş et al., 2006; Pelegrí et al., 2005). In this regard, benthic nepheloid layers (BNLs), turbid bottom layers formed by sediment resuspension and extending several hundred meters above the seafloor, may serve as important pathways for the transfer of margin-derived particles into the deep ocean. A prominent BNL was documented near the Mauritanian margin (Ohnemus and Lam, 2015), supporting the interpretation that shelf sediment remobilization may contribute to the lithogenic particle supply farther offshore, including in the Cabo Verde region.

The Zr/Rb ratios displays a different pattern from Fe/K, with values increasing sharply around ~ 7.5 ka BP (Fig. 7b). This time coincides

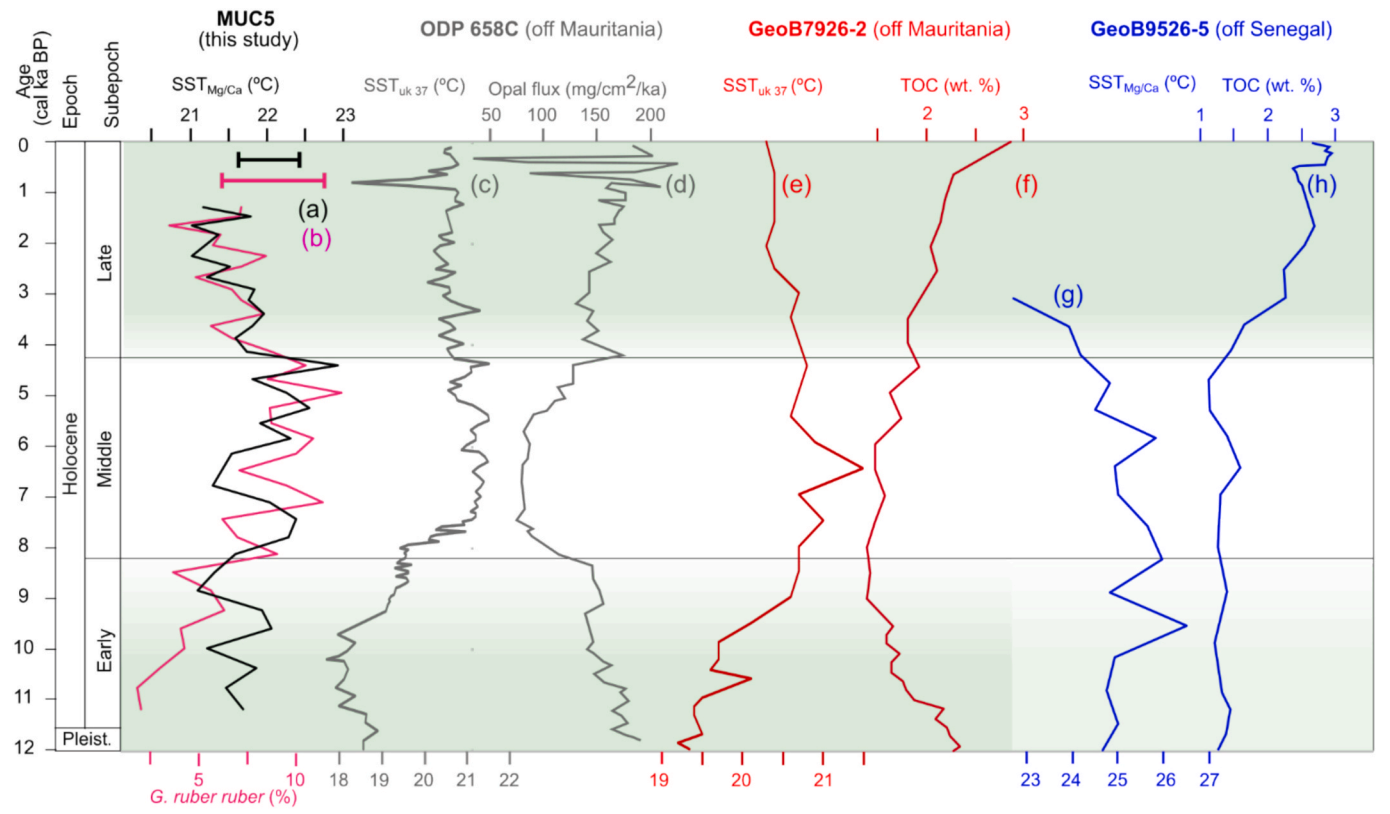

Fig. 9. Comparison of palaeoceanographic proxies from core MUC5 and other sites influenced by Northwest African upwelling. Sites include: MUC5 (seasonal Northwest African upwelling situated in the southeastern rim of the NASTG; this study), ODP Site 658C (permanent Northwest African upwelling, off Mauritania; Zhao et al., 1995; Adkins et al., 2006); GeoB7926-2 (permanent Northwest African upwelling, off Mauritania; Romero et al., 2008a, 2008b) and GeoB9526-5 (seasonal Northwest African upwelling off Senegal; Zarriess and Mackensen, 2010; Zarriess et al., 2011). (a) $SST_{Mg/Ca}$ (black) and (b) relative abundance (%) of *G. ruber ruber* (pink) in MUC5. (c) $SST_{uk\ 37}$ and (d) opal flux (mg/cm^2/ka) at ODP Site 658C. (e) $SST_{uk\ 37}$ and (f) total organic carbon (TOC) in GeoB7926-2. (g) $SST_{Mg/Ca}$ derived from *G. ruber ruber* specimens and (h) TOC in GeoB9526-5. Stronger upwelling, inferred from lower SSTs and higher opal or TOC content, is represented by green shading. Upwelling in the Early Holocene off Senegal (panel g) is not evident; therefore, the shading in that interval is subdued. Horizontal bars = 2σ error.

with the onset of the wettest climatic phase in West Africa, as reported by Tierney et al. (2017). Although Zr may be derived from BNLs, the heavy minerals that host Zr are generally more difficult to transport. Thus, the increase in this ratio may instead reflect heightened humidity over the Cabo Verde islands. This would lead to a greater contribution of sediments rich in volcanic material, and thus in Zr, given the petrological evidence for Zr-bearing minerals in volcanic rocks from the archipelago (e.g., Kogarko et al., 2009). This interpretation is partially supported by studies showing that volcanic lithogenic signatures from Cabo Verde have been geochemically detected in nearby water masses (e.g., Ohnemus and Lam, 2015). However, the interpretation of this proxy remains tentative and should be treated with caution, as is also the case for the Early Holocene.

During this period, the Ca/Ti ratio (Fig. 7c) is relatively low, suggesting reduced carbonate production, potentially due to lower dust-derived fertilisation or diminished upwelling intensity.

The Dry Sahara, from ~ 5.5 ka BP to the top of the core, at ~ 1.3 ka BP: Evidence of increased dust input in MUC5 is indicated by a decline in Fe/K values from ~ 5 ka BP (Fig. 7a), marking the end of the AHP at this site. A rise in dust flux is also observed at ODP Site 658C at ~ 5.5 ka BP (Adkins et al., 2006; deMenocal et al., 2000a, 2000b) (Fig. 7f). In GeoB7926-2, this is reflected in an increase in fine aeolian dust (McKay et al., 2014) (Fig. 7g); while on Brava Island, an increase in the abundance of fine sand suggests intensified erosion under drier conditions at ~ 4 ka BP (Castilla-Beltrán et al., 2021) (Fig. 7h). Visual observations of MUC5 support this environmental transition: a distinct colour change and shift to finer sediments (possibly indicating the deposition of fine aeolian dust) occurs at ~ 12 cm depth (Fig. 4), corresponding to ~ 3.9 ka BP, and such conditions persist up to the core top. The age discrepancies between records may reflect the time-transgressive nature of Saharan aridification, which is known to have occurred earlier in the north than in the south, and in the east before the west (Dallmeyer et al., 2020; deMenocal, 2015).

5.2. Holocene palaeoceanographic variability in the subtropical Northeast Atlantic

5.2.1. Early Holocene

This period is characterized by the dominance of planktonic foraminifera associated with poorly stratified waters (Fig. 8a-c) and by low abundances of species related to warm and stratified conditions (Fig. 8d-f). The Simpson biodiversity index indicates relatively low biodiversity and high dominance (Fig. 8g). SSTs, although fluctuating, appear to be lower (Fig. 8i), which is also supported by the low percentages of *G. ruber ruber*, a taxon with a known affinity for warm waters (Bhadra et al., 2023; Tolderlund and Bé, 1971) (Fig. 9b). SubSSTs are also relatively low (Fig. 8j), consistent with limited advection of warm subsubsurface waters typically associated with the NASTG at this site (see Fig. 2c). This is additionally supported by the low abundances of *G. ruber albus* (Fig. 8f), a species associated with the oligotrophic waters of the subtropical gyres and previously used to trace their influence (Bonfardeci et al., 2018; Reißig et al., 2019; Repschläger et al., 2017). $\delta^{13}C$ values are consistently relatively low in both *G. ruber* s.s. (Wang, 2000) and *G. truncatulinoides* (Supplementary Fig. S3), possibly reflecting the uplift of water masses influenced by AAIW, which is typically poorer in $\delta^{13}C$ (Supplementary Fig. S1; Schmittner et al., 2017).

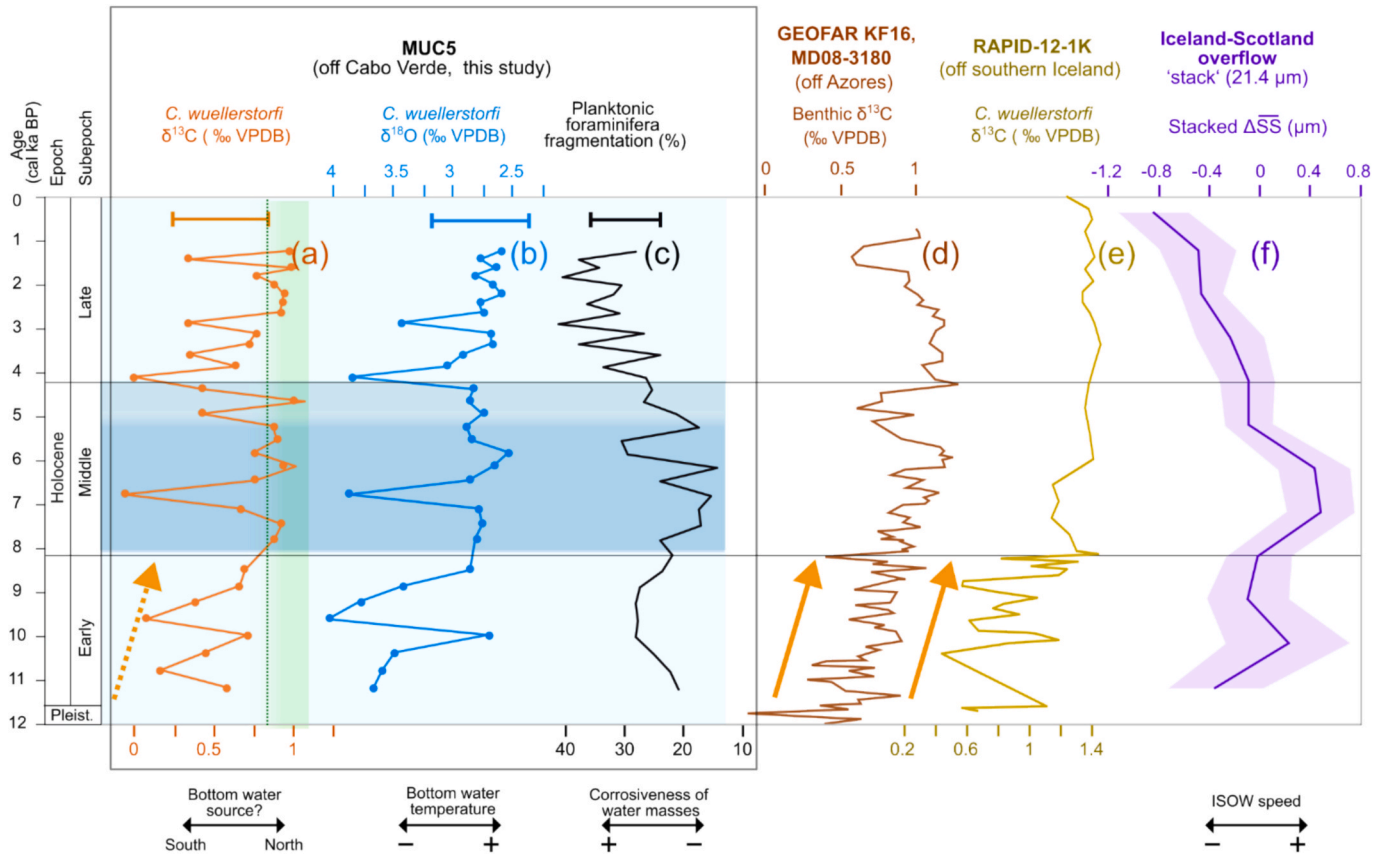

Fig. 10. Characterization of the bottom water mass at MUC5 based on the carbon and oxygen isotopic composition of *C. wuellerstorfi* and planktonic foraminifera fragmentation. The data are compared with other benthic $\delta^{13}C$ records, including GEOFAR KF16 and MD08-3180 (off the Azores; Repschläger et al., 2015), RAPID-12–1 K (off southern Iceland; Thornalley et al., 2010), and the Iceland-Scotland Overflow Water (ISOW) stack curve (Thornalley et al., 2013). (a) *C. wuellerstorfi* $\delta^{13}C$ in MUC5, with typical $\delta^{13}C$ isotopic values of Northeast Atlantic Bottom Water (NEABW) shown in green. (b) *C. wuellerstorfi* $\delta^{18}O$ in MUC5. (c) Planktonic foraminifera fragmentation in MUC5, which reflects the dissolution potential of bottom water masses. Horizontal bars = 2σ error. Darker shadings suggest greater influence of northern-sourced waters, likely dominated by ISOW at this site, though this interpretation remains tentative. (d) Benthic $\delta^{13}C$ (*C. wuellerstorfi* and *Melonis* sp.; ‰ VPDB) in GEOFAR KF16 and MD08-3180, shown as a 3-point running average. (e) *C. wuellerstorfi* $\delta^{13}C$ in RAPID-12–1 K. (f) Stack of sortable silt mean size records associated with ISOW speed from various regional sites. Shaded area = 2σ error.

The hydrographic features described above suggest that well-stratified and warm upper ocean layers, similar to those that develop today during summer (Fig. 1e), did not form in the area during the Early Holocene. This interpretation aligns with the findings of Chapman et al. (1996), based on core BOFS 31 K, located between the coast of Mauritania and the Cabo Verde archipelago (Fig. 1a), who found that modern-like seasonal stratification only became established around 6 ka BP. These differences in seasonal configuration may have been caused by: 1) A year-round upwelling system, rather than the seasonally upwelling observed in the modern regime. 2) A Guinea Dome that was either stronger or had a more northerly centre. The Guinea Dome develops in late summer in this region (Fig. 2d), and changes in its strength or position may have disrupted the thermocline during the period when seasonal stratification would normally intensify.

The cores ODP 658C and GeoB7926-2, both located off Mauritania (Fig. 1a), show evidence of stronger upwelling during the Early Holocene (Adkins et al., 2006; Romero et al., 2008a, 2008b; Zhao et al., 1995) (Fig. 9c-f). In contrast, core GeoB9526, located off Senegal (Fig. 1a), does not exhibit any indicators of enhanced upwelling (Zarriess and Mackensen, 2010; Zarriess et al., 2011) (Fig. 9g-j) during the same interval. If the upwelling system had been stronger or more persistent in the region, a similar signal would be expected in the Senegalese core, which today is affected only by seasonal upwelling, similar to the Cabo Verde region. While the scenario involving a stronger or more centrally located Guinea Dome during the Early Holocene may offer a plausible explanation, it remains uncertain given the relatively limited spatial influence of this feature compared to the broader upwelling system.

5.2.2. Middle Holocene

The Middle Holocene constitutes a transitional subepoch in terms of planktonic foraminifera associations. There is a decrease in the relative abundance of species associated with upwelling or with weak and shallow thermocline conditions (Fig. 8a-c; Supplementary Table S2). Conversely, taxa that increased in relative abundance (Fig. 8d-f) are oligotrophic, warm-water species dwelling in surface or intermediate depths, typically found in subtropical gyres and in distinctly stratified upper ocean waters, which develop during summer in the region (Fig. 1e). Additionally, these faunal changes are accompanied by an increase in planktonic foraminifera biodiversity at ~ 8–7 ka BP, which persists through the rest of the Holocene (Fig. 8g). Here, this observed increase in diversity is attributed to changes in productivity and in the vertical niche structure, caused by the establishment of a seasonality more similar to that of today, either in terms of the annual upwelling pattern or the strength/position of the Guinea Dome.

The Middle Holocene represents the warmest period in both SST and subSST (Fig. 8i-j). These results likely reflect a phase of reduced upwelling and warmer surface conditions, with increased influence from the NASTG. Warm temperatures and reduced upwelling are consistent with other SST and productivity proxy records from Northwest Africa, particularly during the ~ 8–5.5 ka BP interval, both in the region of permanent upwelling (Mauritania; Fig. 9c-f) and in the area influenced

by seasonal upwelling (Senegal; Fig. 9g-h).

Furthermore, the period of lowest surface salinity recorded at ~ 6–7 ka (Fig. 8l) in MUC5 coincides with the maximum rainfall reconstructed by Tierney et al. (2017) (Fig. 7e), suggesting that enhanced precipitation could have freshened the upper ocean layers in the region.

At 4.7 ka BP, a radiolaria bloom was recorded, with an accumulation rate exceeding 20,000 #/cm^2/year (Fig. 8h), indicating a high productivity episode. This is further supported by slight increases in *G. bulloides* (Fig. 8b) and *N. incompta* (Fig. 8c), along with the highest planktonic foraminifera accumulation rate documented within our dataset (Fig. 7d). Considering the low sedimentation rate at the site, this brief event could potentially be linked to the 4.2 ka event (Magny et al., 2007; Thompson et al., 2002; Wanner et al., 2011), characterised by a megadrought that lasted ~ 300 years (Railsback et al., 2018). This drought may have been caused by enhanced dry easterlies, which would cause both upwelling and increased Saharan dust deposition into the ocean, providing silica and other nutrients that could have fertilised the upper water masses and the subsequent proliferation of radiolaria. An alternative hypothesis to explain the radiolaria proliferation could be regional volcanic activity at that time, given the presence of glass shards in this sample (Section 4.2). Although the shards are very rare within this sample, volcanic eruptions can deliver nutrients and increase primary productivity over long distances (Duggen et al., 2007).

5.2.3. Late Holocene

Faunal assemblages became more similar to those observed today, with relatively high percentages of *T. sacculifer* (Fig. 8e) and *G. menardii* (Fig. 8d), reflecting the development of a warm, well stratified surface ocean during summer. However, lower $SSTs_{Mg/Ca}$ (Fig. 9a), together with decreased percentages of *G. ruber ruber* (Fig. 9b), probably suggest enhanced upwelling activity. This configuration likely resembles the modern system, characterised by seasonal upwelling, more intense than during the Middle Holocene, coexisting with a well-developed summer stratification (Fig. 1b-e). Additional evidence for intensified upwelling is observed both in the region of permanent upwelling off Mauritania (Adkins et al., 2006; Romero et al., 2008a, 2008b; Zhao et al., 1995) (Fig. 9c-f) and in the seasonally affected area off Senegal (Zarriess and Mackensen, 2010; Zarriess et al., 2011) (Fig. 9g-h).

In addition, the subSST values (Fig. 8j) and the relatively low abundance of *G. ruber albus* (Fig. 8f) suggest a reduced presence of oligotrophic, warm subsurface waters typically linked to NASTG influence, compared to the Middle Holocene.

At 2.9 ka BP, a notable increase in *G. ruber albus* was noted, reaching 35.8 % relative abundance, compared to the core average of 18.6 % (Fig. 8f), which produced a decline in the biodiversity curve (Fig. 8g). Given the preference of this species for inhabiting the centres of oceanographic gyres and oligotrophic waters, its proliferation may indicate an intensified influence of the NASTG, and a potentially weakened upwelling event. This observation can be tentatively linked to the 2.8 ka event, during which abrupt changes in climate and atmospheric dynamics were triggered by a grand solar minimum (e.g., Martin-Puertas et al., 2012). This may have caused changes in regional wind patterns, briefly altering the oceanographic configuration of the area.

5.3. Holocene bottom water variability based on benthic foraminifera stable isotopes and planktonic foraminiferal fragmentation index

In the tropical Atlantic, NADW co-occurs with the underlying NEABW (Fig. 3), a modified water mass derived from AABW (c.f. Section 2). The latter water mass is restricted from entering the eastern Atlantic due to the Mid-Atlantic Ridge acting as a tectonic barrier (Metcalf et al., 1964) (Supplementary Fig. S1). According to Jenkins et al. (2015), at our study site in the eastern tropical Atlantic, bottom waters bathing the seafloor are composed primarily of ISOW (which forms part of the NADW) and AABW in approximately equal proportions. ISOW is therefore expected to exert a strong influence at this location.

Benthic $\delta^{13}C$ and $\delta^{18}O$ values measured on *C. wuellerstorfi* (Fig. 10) show substantial variability. Most $\delta^{13}C$ values are around 0.8 ‰ VPDB, consistent with those reported from settings influenced by NEABW, typically around ~ 0.8 ‰ or higher (Kuleshova et al., 2022; Pierre et al., 1994; Schmittner et al., 2017) (Supplementary Fig. S1). However, this pattern is interrupted by marked negative excursions reaching ~ 0–0.2 ‰ VPDB, particularly during the Early Holocene, at 6.8 ka BP, and between ~ 5 and 3 ka BP (Fig. 10a). A similar situation is seen in the $\delta^{18}O$ record, where a possible trend toward heavier values is masked by sharp positive peaks rising from baseline values around 2.8 ‰ VPDB up to 3.5–4 ‰ VPDB (Fig. 10b). These anomalies likely reflect the isotopic signature of reworked glacial-age specimens and/or enhanced organic matter input (Mackensen et al., 1993; Zarriess and Mackensen, 2011). Alternatively, the presence of an overall trend among these outliers leaves open the possibility that they reflect short-lived changes in deep water geochemistry. Similar magnitude $\delta^{13}C$ excursions have been reported in other North Atlantic records (e.g., Oppo et al., 2003; Repschläger et al. 2015).

On the other hand, the planktonic foraminifera fragmentation index may be related to carbonate saturation and serve as a proxy for water corrosiveness. A greater proportion of NADW within the NEADW would reduce the influence of AABW and lower the foraminiferal fragmentation index, due to the higher carbonate saturation of North Atlantic-sourced waters compared to those of Antarctic origin (e.g., Liu et al., 2022, and references therein).

During the Early Holocene, $\delta^{13}C$ values at MUC5 are relatively lower, potentially reflecting changes in the composition of northern-sourced waters and/or a greater influence of AABW. The presence of a declining trend in sediment records from the Azores (Repschläger et al., 2015) (Fig. 10d) and south of Iceland (Thornalley et al., 2010) (Fig. 10e) suggests that, at least partially, this shift may have extended from high latitudes to subtropical regions influenced by ISOW. Additionally, the elevated foraminiferal fragmentation index during this period (Fig. 10c) supports enhanced bottom water corrosiveness, likely related to a greater presence of carbonate-undersaturated AABW and/or a diminished ISOW influence. This interpretation is consistent with Thornalley et al. (2013) (Fig. 10f), who report relatively weak ISOW flow during the Early Holocene based on a sortable silt stack from multiple North Atlantic sites. The observed $\delta^{13}C$ depletion at MUC5 during the Early Holocene may thus result from increased AABW influence, a $\delta^{13}C$-depleted northern-sourced component, or a combination of both.

During the Middle Holocene, $\delta^{13}C$ values generally exhibit higher levels and $\delta^{18}O$ values tend to be lower relative to the Early Holocene (Fig. 10a-b). This pattern is consistent with an increased influence of northern-sourced waters, arguably dominated by ISOW, or with changes in their geochemical signature. The $\delta^{13}C$ enrichment observed at MUC5 during this interval is also evident in the records of Repschläger et al. (2015) (Fig. 10d) and Thornalley et al. (2010) (Fig. 10e), suggesting that these changes may have originated in the high-latitude North Atlantic and subsequently propagated to the subtropical eastern Atlantic. Additionally, the planktonic foraminifera fragmentation index shows lower values during the Middle Holocene compared to both the Early and Late Holocene (Fig. 10c). This pattern may reflect an enhanced contribution of NADW (particularly its ISOW component) within the NEABW, relative to AABW. This interpretation is consistent with the sortable silt stack from Thornalley et al. (2013) (Fig. 10f), which indicates increased ISOW strength during this period. Overall, the Middle Holocene appears to reflect a greater contribution of northern-sourced water masses within the NEADW, in agreement with the higher $\delta^{13}C$ values and improved carbonate preservation inferred from the fragmentation index.

The earlier part of the Late Holocene is characterized by reduced $\delta^{13}C$ and heavier $\delta^{18}O$ values (Fig. 10a-b). From ~ 2.5 ka BP onward, isotopic values return to levels more typical of NEADW. This variability is not observed in the $\delta^{13}C$ records of Repschläger et al. (2015) and Thornalley et al. (2010), suggesting that the signal at MUC5 may reflect

local processes. One possibility is the presence of reworked glacial specimens; alternatively, it may indicate a transient increase in AABW influence reaching subtropical latitudes during the lower part of the Late Holocene, without extending to higher latitudes. More broadly, the Late Holocene is also marked by elevated planktonic foraminifera fragmentation index values (Fig. 10c), suggesting increased bottom water corrosiveness. This pattern may be linked to a stronger contribution of AABW and/or a reduced presence of northern-sourced waters within the NEABW. This interpretation is further supported by the sortable silt stack of Thornalley et al. (2013) (Fig. 10f), which shows a similar trend to the fragmentation index, and indicates a weakening of ISOW flow during the Late Holocene.

However, the above interpretations remain tentative and should be viewed with caution, given the potential overlap of different water mass signals and preservation effects. Further, the elevated planktonic foraminiferal fragmentation observed during the Early and Late Holocene could also reflect enhanced upwelling in the region (see Section 5.2), rather than reduced North Atlantic-sourced deep waters influence. The upwelling could elevate organic carbon levels, which, upon deep remineralization, may have contributed to increased fragmentation. Zarriess and Mackensen (2010) similarly report strong carbonate dissolution at site GeoB9526-5 during the Late Holocene, which they attribute to elevated fluxes of organic matter to the seafloor.

Further sedimentological and benthic geochemical analyses would help to better constrain Holocene deep-water variability in this region.

5.4. Holocene dynamics of the North Atlantic subtropical gyre (NASTG) and broader climate linkages

5.4.1. Holocene changes in the NASTG and the delayed appearance of Globorotalia menardii

Several records across the NASTG reveal considerable spatial and temporal variability throughout the Holocene (Fig. 11a-j). During the Early Holocene, core MUC5 shows a clear predominance of species that thrive in poorly stratified waters, in contrast to those associated with warm and well-stratified upper ocean layers (this study; Fig. 11a-b), as well as cooler subSST (Fig. 8j), suggesting reduced influence of the NASTG and its associated warm subsurface waters (Fig. 2c). In contrast, sites off Tobago (core M78/1_235-1; Nürnberg et al., 2020; Reißig et al., 2019) and in the southeastern Caribbean (core VM12-107; Schmidt et al., 2012) exhibit higher subSST$_{Mg/Ca}$ values at the base of the Early Holocene, indicative of warmer subsurface waters that progressively cooled over this sub-epoch (Fig. 11c-d). Core GA307-Win-12GC (Fischel et al., 2017; Fig. 11e), located in the western NASTG, shows relatively low stratification, according to the relatively high proportions of subsurface-dwelling planktonic foraminifera. At ODP Site 1063, lower

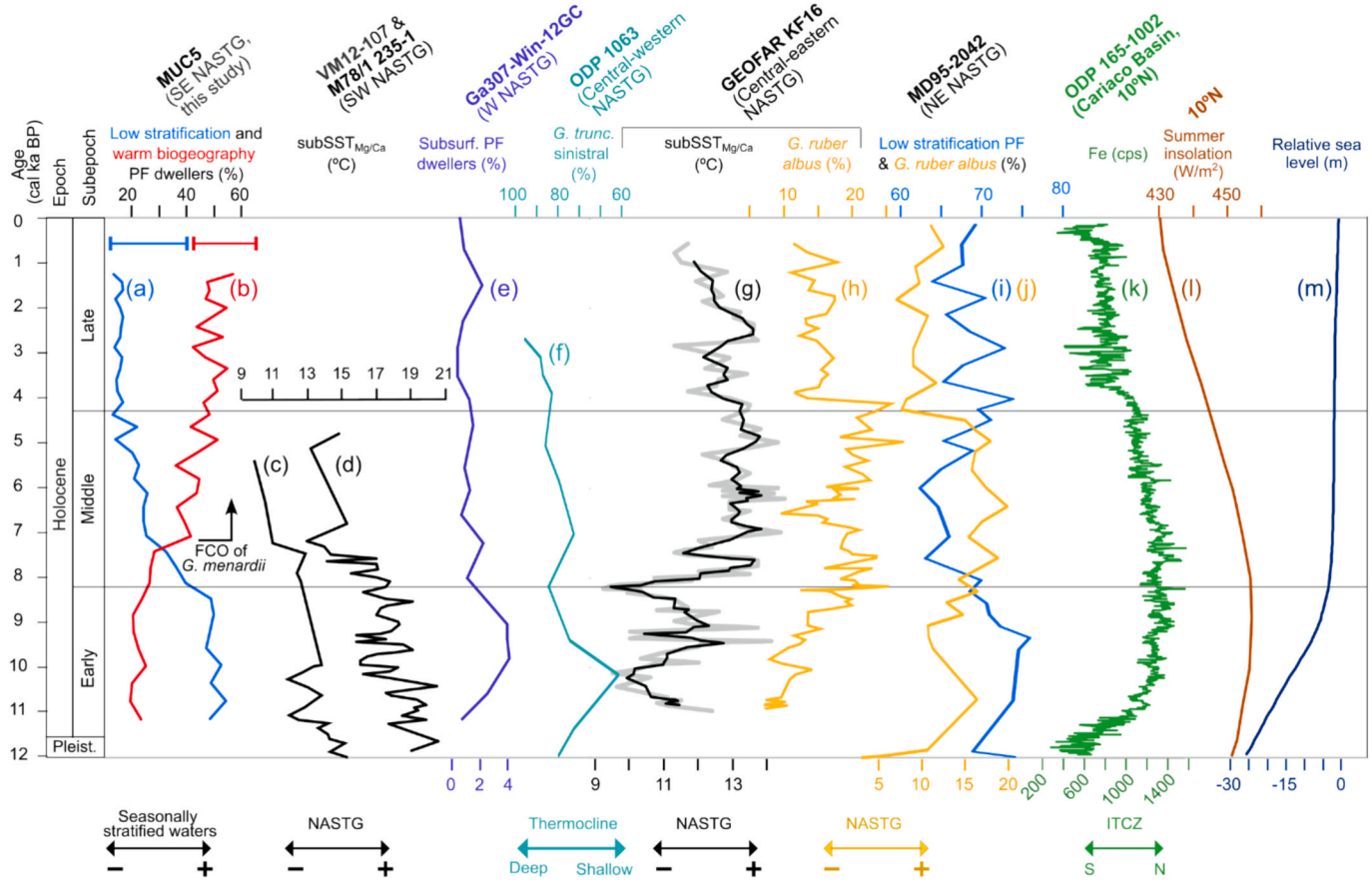

Fig. 11. Comparison of palaeoceanographic proxies from different sites across the North Atlantic Subtropical Gyre (NASTG) alongside potential forcing mechanisms. (a) Relative abundance of upwelling and/or poorly stratified water species in MUC5 (this study). (b) Relative abundance of warm-water planktonic taxa in MUC5, as classified by Brummer and Kučera (2022) (this study). Note that the first common occurrence (FCO) of *G. menardii* does not take place until warm-water taxa become dominant. Horizontal bars in b and c = 2σ error. (c) SubSST$_{Mg/Ca}$ derived from *Globorotalia crassaformis* in core VM12-107 (Schmidt et al., 2012). (d) SubSST$_{Mg/Ca}$ derived from *G. truncatulinoides* in core M78/1_235-1 (Nürnberg et al., 2020; Reißig et al., 2019). (e) Relative abundance of subsurface planktonic foraminifera at Ga307-Win-12GC (Fischel et al., 2017). (f) Relative abundance of *G. truncatulinoides* (sinistral) at ODP Site 1063 (Billups et al., 2016, 2020). (g) subSST$_{Mg/Ca}$ derived from *G. truncatulinoides* in core GEOFAR KF16 (Repschläger et al., 2017). (h) Relative abundance of *G. ruber albus* in GEOFAR KF16 (Repschläger et al., 2017). (i) Relative abundance of species indicative of poorly stratified waters (*N. incompta*, *G. inflata* and *G. bulloides*) and (j) of *G. ruber albus* in MD95-2042 (Rossignol, 2022). (k) Fe abundance in ODP Site 165–1002 (Haug et al., 2001a, 2001b), used as a proxy for the meridional latitudinal migration of the ITCZ. (l) Summer insolation at 10°N (Laskar et al., 2004). (m) Relative sea level (de Boer et al., 2014).

relative abundances of *G. truncatulinoides* sinistral suggest a shallower thermocline (Billups et al., 2016, 2020; Fig. 11f). In the eastern subtropical Atlantic, both $subSST_{Mg/Ca}$ values and the abundance of the gyre indicator *G. ruber albus* are low at GEOFAR KF16 (Repschläger et al., 2017; Fig. 11g-h), following patterns that closely resemble those of MUC5 in both magnitude and trend (Fig. 8f; Fig. 8j). Similarly, core MD95-2042 (Rossignol, 2022) shows increased abundances of species associated with poorly stratified waters and low proportions of *G. ruber albus* (Fig. 11i-j). Altogether, these records suggest that during the Early Holocene, the hydrographic configuration of the NASTG differed from today, with subsurface warming in the southeastern Caribbean and Tobago Basin, reduced stratification in the western and central sectors, and cooler, less stratified subsurface waters in the east.

The Middle Holocene is characterized by relatively warm and stable oceanic conditions, primarily driven by orbitally induced increases in Northern Hemisphere summer insolation (e.g., Kaufman, 2004; Kaufman et al., 2020). Despite these generally warm and stable conditions, the delayed proliferation of *G. menardii* in the Atlantic remains a notable and unresolved feature of this subepoch. This warm-water species was absent or extremely rare during glacial periods, reappearing during interglacials (Ericson and Wollin, 1968). Nevertheless, it becomes a significant component of Atlantic Holocene planktonic foraminifera assemblages around 7.5 ka BP (Broecker and Pena, 2014), indicating a notable delay following the end of the last glacial period. At MUC5, *G. menardii* reaches substantial abundances only between 7.4 and 7.1 ka BP (Figs. 8d, 11b), in agreement with this timing. Several hypotheses have been proposed to explain this delayed reappearance. One suggests a re-seeding from the Indian Ocean, potentially facilitated by intensified Agulhas leakage (Berger and Vincent, 1986; Berger and Wefer, 1996). Another line of reasoning attributes the delay to unsuitable hydrographic conditions in the Atlantic itself (Broecker and Pena, 2014; Sexton and Norris, 2011). As a symbiont-bearing species restricted to a narrow depth range within the thermocline (Steph et al., 2009), *G. menardii* is particularly sensitive to changes in upper ocean structure (Besiou et al., 2023). During the Early Holocene, our study site was characterized by weak surface stratification and a shallow thermocline, consistent with patterns observed elsewhere across the NASTG, as previously discussed. Therefore, we favour the interpretation that *G. menardii* was unable to establish viable populations in the North Atlantic due to oceanographic conditions that were not conducive to its persistence. Notably, although *G. menardii* reaches some of its highest abundances today in the eastern subtropical Atlantic (e.g., Caley et al., 2012), it was nearly absent there during the Early Holocene, when upper-layer stratification differed considerably from modern conditions, and its abundance began to increase gradually during the Middle Holocene as oceanographic conditions became more favourable. In contrast, occurrences of *G. menardii* as early as 11 ka BP have been documented in the Caribbean (Hüls and Zahn, 2000), suggesting that warm subsurface conditions in the southwestern gyre may have provided suitable habitats earlier than in the east.

In the Late Holocene, subSST values decrease at MUC5 (Fig. 8j) and GEOFAR KF16 (Fig. 11g), suggesting a reduced influence of the NASTG and its associated warm waters in the temperate eastern part of the central and southern sectors of the gyre (Fig. 2c). Additionally, the decline in *G. ruber albus* abundance at MUC5 (Fig. 8f), GEOFAR KF16 (Fig. 11h), and MD95-2042 (Fig. 11j) further supports this interpretation.

5.4.2. Drivers of Holocene oceanographic variability in the subtropical Northeast Atlantic

During the Early Holocene, SSTs in the subtropical Northeast Atlantic were relatively low (Fig. 9a-b), and well-stratified summer surface waters were poorly developed, as indicated by the high relative abundance of planktonic foraminifera associated with weakly stratified conditions (Fig. 11a). The Fe/K ratio (Fig. 7a) reflects humidity variations in a pattern similar to the reconstructed latitudinal shifts of the ITCZ from the Cariaco Basin (Haug et al., 2001a, 2001b; Fig. 11k) in ODP site 165–1002 (Fig. 1a). Both records indicate arid conditions during the Preboreal (until ~ 10 ka BP), followed by a relatively rapid increase in humidity. Rainfall reconstructions from Tierney et al. (2017) (Fig. 7e) indicate relatively high precipitation during the Early Holocene, particularly between ~ 11 and 9 ka BP. The coexistence of relatively cool SSTs and high precipitation departs from the modern seasonal pattern, where increased rainfall is linked to a northward-shifted ITCZ, an intensified West African Monsoon, reduced upwelling and warmer SSTs. In contrast, our data suggest strong upwelling and/or enhanced Guinea Dome activity occurring simultaneously with elevated rainfall during at least some intervals of the Early Holocene. This subepoch coincides with a precession minimum and peak summer insolation at 10°N (Fig. 11l) and therefore, the intensified boreal summer insolation appears to have been the primary driver of this climatic configuration. The differing seasonal insolation patterns in both hemispheres likely influenced atmospheric dynamics and contributed to changes in ice volume and relative sea level, which approached near-modern values only around the transition between the Early and Middle Holocene (Fig. 11m). These changes likely triggered large-scale shifts in ocean–atmosphere circulation, resulting in a distinct climatic configuration. One possible scenario is a La Niña-like background state during the Early Holocene. Proxy records indicate warm SSTs in the Gulf of Guinea (Weldeab et al., 2007), while our site shows cooler SSTs and strong upwelling in the subtropical Atlantic, along with increased rainfall in Northwest Africa. These three patterns are consistent with modern La Niña-like conditions (Rowell, 2001; Yamoula et al., 2025). This view of the Early Holocene climate as a La Niña-like state is further supported by model simulations (Liu et al., 2003) and proxy records indicating a very low number of El Niño events compared to the rest of the Holocene (Moy et al., 2002).

During the Middle Holocene, warm SSTs and well-stratified surface waters during summer gradually intensified in the northeastern subtropical Atlantic. Humidity proxies (Fe/K; Fig. 7a) suggest sustained high moisture levels until ~ 5.5 ka BP, consistent with rainfall reconstructions from Tierney et al. (2017) (Fig. 7e) and a persistently northward-displaced ITCZ (Haug et al., 2001a, 2001b; Fig. 11k). This configuration resembles the modern seasonal analogue, in which weaker easterly winds and a northward-shifted ITCZ reduce upwelling intensity and allow southwesterly trade winds to penetrate farther into Northwest Africa, enhancing rainfall and vegetation expansion characteristic of the AHPs (e.g., Bradtmiller et al., 2016). These conditions were likely driven by astronomically forced insolation (Fig. 11l), together with the stabilization of relative sea level (Fig. 11m), and support the broader view of a progressive reorganization of the North Atlantic system toward a modern-like configuration during the Early-Middle Holocene transition (e.g., Hillaire-Marcel et al., 2001; Thornalley et al., 2010). Furthermore, a rising number of El Niño events (Moy et al., 2002) marks a shift toward a climate system more similar to modern conditions.

In the deep ocean at the site, a possibly increase in NEADW relative to AABW appears to coincide with enhanced ISOW strength during the Middle Holocene (Thornalley et al., 2013) (c.f. Section 5.3), along with periods of increased rainfall recorded off Cape Blanc (Fig. 7e; Tierney et al., 2017). While our interpretation remains tentative, previous studies have proposed that ISOW variability may be linked to different Atlantic climate modes (Lohmann et al., 2015; Mjell et al., 2016) and correlated with shifts in Saharan dust production (Cruz et al. 2021), which is consistent with the observed coupling between changes in deep water composition and regional climate at our study site.

During the Late Holocene, seasonally well-stratified surface waters became established at levels comparable to those of today, with high and stable proportions of warm-water dwellers (Fig. 11b) and relatively cool SSTs (Fig. 9a-b). Increased aridity, as indicated by Fe/K ratios (Fig. 7a), coincides with a southward-displaced ITCZ (Fig. 11k) and reduced monsoon activity (Fig. 7e), consistent with the modern seasonal analogue. In this configuration, strong trade winds and a southward-

shifted ITCZ would enhance upwelling, cooling SSTs, and limiting moisture availability, further contributing to drier conditions (Weldeab et al., 2005). Precessional forcing (Fig. 11l) likely continued to play a key role in shaping seasonal variability, inducing the southward migration of the ITCZ in this area and shaping regional oceanographic conditions.

The regional oceanographic dynamics of the subtropical Northeast Atlantic demonstrate marked variability, even during the relatively stable climate of the Holocene. Changes in upwelling intensity and in the characteristics of the NASTG can alter nutrient supply and the vertical structure of the water column, ultimately impacting the composition of marine communities. These findings underscore the importance of understanding the drivers of variability in this dynamic upwelling ecosystem, which is part of a highly complex climate-ocean-continent system sensitive to both global and regional forcings.

6. Conclusions

1. Profiles of chemical compositions produced by XRF scans of MUC5, planktonic foraminifera accumulation rates, and sediment descriptions, identify major Holocene climate phases, including a dry Preboreal, the African Humid Period starting at ~ 10 ka BP, and the onset of aridity at ~ 5.5 ka BP, with fully dry conditions likely established by ~ 4 ka BP. The inverse relationship between Fe/K ratios and both Ca/Ti ratios and planktonic foraminifera accumulation rates suggest that humid periods were linked to reduced biogenic carbonate production in the area
2. Microfossil assemblages and isotopic data from core MUC5 indicate that the Early Holocene was characterized by a water column lacking modern-like seasonal stratification in the region, likely due to year-round upwelling (as opposed to the present-day seasonal pattern) or a more dominant Guinea Dome. The Middle Holocene reflects a transitional phase, based on faunal assemblages transitional between those of the Early and Late Holocene, which indicate emerging seasonality in water column stratification. This interval also shows evidence of reduced upwelling and greater presence of warm subsurface waters associated with the NASTG. The Late Holocene is characterized by cooler SST and subSSTs conditions, but shows a dominance of species indicative of strong summer stratification, consistent with the establishment of a seasonal upwelling regime similar to the modern system in the region. These shifts in seasonal stratification throughout the Holocene were likely paced by the broader climatic background set by changes in precession
3. During the Early Holocene, the hydrographic configuration of the NASTG differed from today, with subsurface warming in its southwestern sector, reduced stratification in the western and central parts, and cooler, less stratified subsurface waters in the east. These patterns suggest that, during this interval, warm subsurface waters typically associated with the NASTG were more prevalent in the western than in the eastern portion of its southern sector, relative to later periods. A subsequent increase in the influence of these subsurface waters is inferred for the eastern sector during the Middle Holocene, followed by a reduction in this influence during the Late Holocene
4. Benthic proxies suggest that the composition of the NEABW (resulting from a mixture of AABW and northern-sourced waters, arguably primarily ISOW at this latitude) varied throughout the Holocene, although interpretations remain tentative. During the Early Holocene, depleted $\delta^{13}C$ values may reflect a reduced contribution of northern-sourced waters relative to AABW. This interpretation is supported by increased planktonic foraminiferal fragmentation, indicating more corrosive bottom waters. Alternatively, the northern-sourced component itself may have been isotopically lighter at that time. In the Middle Holocene, higher $\delta^{13}C$ values suggest either a greater influence of northern-sourced waters, consistent with lower fragmentation, or a progressive $\delta^{13}C$ enrichment within that component. In the Late Holocene, increased fragmentation again points to more corrosive conditions, potentially reflecting a decreased contribution of northern-sourced waters to the NEABW
5. Our results suggest that, throughout the Middle and Late Holocene, arid phases in Northwest Africa were associated with enhanced upwelling, while humid phases tended to coincide with reduced upwelling and increased influence of the NASTG. This relationship may reflect shifts in the latitudinal position of the ITCZ, with its northward position favouring warmer, more stratified conditions and intensified monsoon activity, and its southward displacement linked to stronger northeasterly trade winds, enhanced upwelling, and cooler SSTs. However, this pattern does not hold during the Early Holocene, when continental humidity coexisted with low SSTs, likely due to intensified upwelling. These discrepancies suggest that larger-scale mechanisms may have been at play. In particular, our results are consistent with a La Niña-like state during the Early Holocene. High-latitude teleconnections, possibly associated with broader climate reorganizations, and internal land-surface feedbacks may have contributed to the onset and maintenance of the AHP during this subepoch
6. Altogether, our findings underscore the complexity of ocean–atmosphere-continent interactions and highlight the value of integrating past variability to better understand future changes in the subtropical Northeast Atlantic. Even under the relatively stable climatic conditions of the Holocene, this region experienced significant shifts in oceanographic and planktonic foraminiferal community structure. This is particularly relevant given the presence of an upwelling system that sustains key marine ecosystems and the human communities that depend on them

Declaration of Generative AI and AI-assisted technologies in the writing process

During the preparation of this work, IPR used ChatGPT to assist in refining the language and improving readability. After using this tool, the author reviewed and edited the content as needed and takes full responsibility for the content of the publication.

CRediT authorship contribution statement

Irene Pérez-Rodríguez: Writing – review & editing, Writing – original draft, Visualization, Validation, Methodology, Investigation, Conceptualization. **Dirk Nürnberg:** Writing – review & editing, Writing – original draft, Supervision, Methodology, Investigation, Conceptualization. **Julie C. Schindlbeck-Belo:** Writing – review & editing, Writing – original draft, Visualization, Methodology, Investigation. **Jack H. Wharton:** Writing – review & editing, Writing – original draft, Investigation. **Thor H. Hansteen:** Writing – review & editing, Methodology, Funding acquisition, Conceptualization. **Veerle A.I. Huvenne:** Writing – review & editing, Methodology, Funding acquisition, Conceptualization. **David J.R. Thornalley:** Writing – review & editing, Investigation. **Ángela Mosquera Giménez:** Writing – review & editing, Investigation. **Steffen Kutterolf:** Writing – review & editing, Methodology. **Kelsey Archer Barnhill:** Writing – review & editing, Methodology. **Covadonga Orejas:** Writing – review & editing, Project administration, Methodology, Funding acquisition, Conceptualization.

Declaration of competing interest

The authors declare that they have no known competing financial interests or personal relationships that could have appeared to influence the work reported in this paper.

Acknowledgments

The research included in this manuscript received funding from the European Union's Horizon 2020 iAtlantic project (Grant Agreement No. 818123). This manuscript reflects the authors' view alone, and the European Union cannot be held responsible for any use that may be made of the information contained herein. This work received funding through the Study Group "Deep-sea benthic ecosystems offshore West Africa" led by V.A.I. Huvenne and C. Orejas, supported by the HWK for the concept development of this manuscript. We would like to express our gratitude to the crew, the technicians from UTM CSIC, and the scientific team aboard the RV Sarmiento de Gamboa for their help both onboard and during the preparation of the iMirabilis2 expedition. Ship time was provided by the Spanish Ministry of Science and Innovation. Special thanks to Beatriz Vinha, Andrea Gori, Susan Evans, and Erik Simon-Lledó for their assistance during sampling, and to Manuel Casas Gallego for his efforts in attempting to obtain palynomorphs from the samples. We are grateful to Olivia Zöller (Institute of Geosciences, CAU Kiel) for her valuable guidance while conducting XRF core scanning. IPR is also indebted to C. Devey (GEOMAR), who hosted her as an invited scientist to perform part of the analyses presented here. We thank the anonymous reviewers for their thorough and constructive feedback, which significantly improved the quality and clarity of this manuscript.

Sample availability

Core MUC5 is stored in the GEOMAR core and rock repository (https://www.geomar.de/en/centre/central-facilities/tlz/core-rock-repository) and can be made available upon request by contacting geosamples@geomar.de.

Appendix A. Supplementary data

Supplementary data to this article can be found online at https://doi.org/10.1016/j.pocean.2025.103578.

Data availability

All datasets generated during this study are available in the PANGAEA repository and cited in the reference list (Pérez-Rodríguez et al., 2024a–e): https://doi.org/10.1594/PANGAEA.972427, https://doi.org/10.1594/PANGAEA.972513, https://doi.org/10.1594/PANGAEA.972509, https://doi.org/10.1594/PANGAEA.972511, https://doi.org/10.1594/PANGAEA.972512.

References

Adkins, J., deMenocal, P., Eshel, G., 2006. The "African humid period" and the record of marine upwelling from excess ^{230}Th in Ocean Drilling Program Hole 658C. Paleoceanography 21 (4), PA4203. https://doi.org/10.1029/2005PA001200.

Armstrong, E., Tallavaara, M., Hopcroft, P.O., Valdes, P.J., 2023. North African humid periods over the past 800,000 years. Nat. Commun. 14, 5549. https://doi.org/10.1038/s41467-023-41219-4.

Arz, H.W., Pätzold, J., Wefer, G., 1998. Correlated Millennial-Scale Changes in Surface Hydrography and Terrigenous Sediment Yield Inferred from Last-Glacial Marine Deposits off Northeastern Brazil. Quat. Res. 50 (2), 157–166. https://doi.org/10.1006/qres.1998.1992.

Aubry, M.-P., Van Couvering, J.A., Christie-Blick, N., Landing, E., Pratt, B.R., Owen, D.E., Ferrusquía-Villafranca, I., 2009. Terminology of geological time: Establishment of a community standard. Stratigraphy 6 (2), 100–105. https://doi.org/10.29041/strat.06.2.04.

Bemis, B.E., Spero, H.J., Bijma, J., Lea, D.W., 1998. Reevaluation of the oxygen isotopic composition of planktonic foraminifera: Experimental results and revised paleotemperature equations. Paleoceanography 13 (2), 150–160. https://doi.org/10.1029/98PA00070.

Berger, W.H., Vincent, E., 1986. Sporadic shutdown of North Atlantic deep water production during the Glacial–Holocene transition? Nature 324 (6), 53–55. https://doi.org/10.1038/324053a0.

Berger, W.H., Wefer, G., 1996. Expeditions into the past: Paleoceanographic studies in the South Atlantic, in: Wefer, Gerold, Berger, W.H., Siedler, G., Webb, D.J. (Eds.), The South Atlantic: Present and Past Circulation. Springer-Verlag, Berlin, Heidelberg, pp. 363–410.

Besiou, E., Kontakiotis, G., Vasiliev, I., Moissette, P., Cornée, J.-J., Antonarakou, A., 2023. Evolutionary Palaeoecological and Morphological Response of *Globorotalia menardii* to Environmental Stress Conditions Preceding the Tortonian–Messinian Boundary in the Mediterranean Basin. Journal of Marine Science and Engineering 11 (6), 1228. https://doi.org/10.3390/jmse11061228.

Bhadra, S.R., Saraswat, R., Kumar, G., Suokhrie, T., 2023. Revisiting the Biostratigraphic Range and Possible Cause of the First and Last Occurrence of *Globigerinoides Ruber* (Pink) in the Northern Indian Ocean. J. Foramin. Res. 53 (2), 120–130. https://doi.org/10.2113/gsjfr.53.2.120.

Biasutti, M., 2019. Rainfall trends in the African Sahel: Characteristics, processes, and causes. WIREs Clim. Change 10 (4), e591.

Billups, K., Hudson, C., Kunz, H., Rew, I., 2016. Exploring *Globorotalia truncatulinoides* coiling ratios as a proxy for subtropical gyre dynamics in the northwestern Atlantic Ocean during late Pleistocene Ice Ages: *Globorotalia Truncatulinoides* Coiling. Paleoceanography 31 (5), 553–563. https://doi.org/10.1002/2016PA002927.

Billups, K., Scheinwald, A., 2014. Origin of millennial-scale climate signals in the subtropical North Atlantic. Paleoceanography 29 (6), 612–627. https://doi.org/10.1002/2014PA002641.

Billups, K., Vizcaíno, M., Chiarelli, J., Kaiser, E.A., 2020. NOAA/WDS Paleoclimatology - North Atlantic Ocean Western Boundary Current Globorotalia truncatulinoides Coiling Ratio Data for the past 700 kyr. 10.25921/F0B2-DC47.

Blanchet, C.L., Tjallingii, R., Frank, M., Lorenzen, J., Reitz, A., Brown, K., Feseker, T., Brückmann, W., 2013. High- and low-latitude forcing of the Nile River regime during the Holocene inferred from laminated sediments of the Nile deep-sea fan. Earth Planet. Sci. Lett. 364, 98–110. https://doi.org/10.1016/j.epsl.2013.01.009.

Bond, G., Kromer, B., Beer, J., Muscheler, R., Evans, M.N., Showers, W., Hoffmann, S., Lotti-Bond, R., Hajdas, I., Bonani, G., 2001. Persistent Solar Influence on North Atlantic Climate During the Holocene. Science 294, 2130–2136. https://doi.org/10.1126/science.1065680.

Bonfardeci, A., Caruso, A., Bartolini, A., Bassinot, F., Blanc-Valleron, M.-M., 2018. Distribution and ecology of the *Globigerinoides ruber — Globigerinoides elongatus* morphotypes in the Azores region during the late Pleistocene-Holocene. Palaeogeogr. Palaeoclimatol. Palaeoecol. 491, 92–111. https://doi.org/10.1016/j.palaeo.2017.11.052.

Bourlès, B., Andrié, C., Gouriou, Y., Eldin, G., Du Penhoat, Y., Freudenthal, S., Dewitte, B., Gallois, F., Chuchla, R., Baurand, F., Aman, A., Kouadio, G., 2003. The deep currents in the Eastern Equatorial Atlantic Ocean. Geophys. Res. Lett. 30 (5), 2002GL015095. https://doi.org/10.1029/2002GL015095.

Bowie, A.R., Maldonado, M.T., Frew, R.D., Croot, P.L., Achterberg, E.P., Mantoura, R.F.C., Worsfold, P.J., Law, C.S., Boyd, P.W., 2001. The fate of added iron during a mesoscale fertilisation experiment in the Southern Ocean. Deep Sea Res. Part II 48 (11–12), 2703–2743. https://doi.org/10.1016/S0967-0645(01)00015-7.

Boyle, E.A., Keigwin, L.D., 1985. Comparison of Atlantic and Pacific paleochemical records for the last 215,000 years: changes in deep ocean circulation and chemical inventories. Earth Planet. Sci. Lett. 76 (1–2), 135–150. https://doi.org/10.1016/0012-821X(85)90154-2.

Boyle, E.A., Rosenthal, Y., 1996. Chemical hydrography of the South Atlantic during the Last Glacial Maximum: Cd vs. δ^{13}C. In: Wefer, G., Siedler, G., Webb, D. (Eds.), The South Atlantic: Present and Past Circulation. Springer, Berlin, Heidelberg, pp. 423–443.

Bradtmiller, L.I., McGee, D., Awalt, M., Evers, J., Yerxa, H., Kinsley, C.W., deMenocal, P.B., 2016. Changes in biological productivity along the northwest African margin over the past 20,000 years. Paleoceanography 31 (1), 185–202. https://doi.org/10.1002/2015PA002862.

Broecker, W., Pena, L.D., 2014. Delayed Holocene reappearance of *G. menardii*. Paleoceanography 29 (4), 291–295. https://doi.org/10.1002/2013PA002590.

Broecker, W.S., Klas, M., Clark, E., Bonani, G., Ivy, S., Wolfli, W., 1991. The Influence of $CaCO_3$ Dissolution on Core Top Radiocarbon Ages for Deep-Sea Sediments. Paleoceanography 6 (5), 593–608. https://doi.org/10.1029/91PA01768.

Brummer, G.-J.-A., Kučera, M., 2022. Taxonomic review of living planktonic foraminifera. J. Micropalaeontol. 41 (1), 29–74. https://doi.org/10.5194/jm-41-29-2022.

Caley, T., Giraudeau, J., Malaizé, B., Rossignol, L., Pierre, C., 2012. Agulhas leakage as a key process in the modes of Quaternary climate changes. Proc. Natl. Acad. Sci. 109 (18), 6835–6839. https://doi.org/10.1073/pnas.1115545109.

Carlson, A.E., LeGrande, A.N., Oppo, D.W., Came, R.E., Schmidt, G.A., Anslow, F.S., Licciardi, J.M., Obbink, E.A., 2008. Rapid early Holocene deglaciation of the Laurentide ice sheet. Nat. Geosci. 1, 620–624. https://doi.org/10.1038/ngeo285.

Castilla-Beltrán, A., De Nascimento, L., Fernández-Palacios, J.M., Whittaker, R.J., Romeiras, M.M., Cundy, A.B., Edwards, M., Nogué, S., 2021. Effects of Holocene climate change, volcanism and mass migration on the ecosystem of a small, dry island (Brava, Cabo Verde). J. Biogeogr. 48 (6), 1392–1405. https://doi.org/10.1111/jbi.14084.

Chandan, D., Peltier, W.R., 2020. African Humid Period Precipitation Sustained by Robust Vegetation, Soil, and Lake Feedbacks. Geophys. Res. Lett. 47 (21), e2020GL088728. https://doi.org/10.1029/2020GL088728.

Chapman, M.R., Shackleton, N.J., Zhao, M., Eglinton, G., 1996. Faunal and alkenone reconstructions of subtropical North Atlantic surface hydrography and paleotemperature over the last 28 kyr. Paleoceanography 11 (3), 343–357. https://doi.org/10.1029/96PA00041.

Cheddadi, R., Carré, M., Nourelbait, M., François, L., Rhoujjati, A., Manay, R., Ochoa, D., Schefuß, E., 2021. Early Holocene greening of the Sahara requires Mediterranean winter rainfall. Proc. Natl. Acad. Sci. 118 (23), e2024898118. https://doi.org/10.1073/pnas.2024898118.

Cléroux, C., Cortijo, E., Anand, P., Labeyrie, L., Bassinot, F., Caillon, N., Duplessy, J.-C., 2008. Mg/Ca and Sr/Ca ratios in planktonic foraminifera: Proxies for upper water

column temperature reconstruction. Paleoceanography 23 (3), PA3214. https://doi.org/10.1029/2007PA001505.
Cléroux, C., Debret, M., Cortijo, E., Duplessy, J.-C., Dewilde, F., Reijmer, J., Massei, N., 2012. High-resolution sea surface reconstructions off Cape Hatteras over the last 10 ka. Paleoceanography 27 (1), PA1205. https://doi.org/10.1029/2011PA002184.
Collins, J.A., Schefuß, E., Heslop, D., Mulitza, S., Prange, M., Zabel, M., Tjallingii, R., Dokken, T.M., Huang, E., Mackensen, A., Schulz, M., Tian, J., Zarriess, M., Wefer, G., 2011. Interhemispheric symmetry of the tropical African rainbelt over the past 23,000 years. Nat. Geosci. 4 (1), 42–45. https://doi.org/10.1038/ngeo1039.
Cropper, T.E., Hanna, E., Bigg, G.R., 2014. Spatial and temporal seasonal trends in coastal upwelling off Northwest Africa, 1981–2012. Deep Sea Res. Part I 86, 94–111. https://doi.org/10.1016/j.dsr.2014.01.007.
Croudace, I.W., Rothwell, R.G., 2015. Twenty Years of XRF Core Scanning Marine Sediments: What Do Geochemical Proxies Tell Us? In: Croudace, I.W., Rothwell, R.G. (Eds.), Micro-XRF Studies of Sediment Cores: Applications of a Non-Destructive Tool for the Environmental Sciences, Developments in Paleoenvironmental Research. Springer, Netherlands, Dordrecht, pp. 25–102. https://doi.org/10.1007/978-94-017-9849-5.
Cruz, J.A., McDermott, F., Turrero, M.J., Edwards, R.L., Martín-Chivelet, J., 2021. Strong links between Saharan dust fluxes, monsoon strength, and North Atlantic climate during the last 5000 years. Sci. Adv. 7 (26), eabe6102. https://doi.org/10.1126/sciadv.abe6102.
Dallmeyer, A., Claussen, M., Lorenz, S.J., Shanahan, T., 2020. The end of the African humid period as seen by a transient comprehensive Earth system model simulation of the last 8000 years. Clim. Past 16 (1), 117–140. https://doi.org/10.5194/cp-16-117-2020.
de Boer, B., Lourens, L.J., Van De Wal, R.S.W., 2014. Persistent 400,000-year variability of Antarctic ice volume and the carbon cycle is revealed throughout the Plio-Pleistocene. Nat. Commun. 5 (1), 2999. https://doi.org/10.1038/ncomms3999.
Dekens, P.S., Lea, D.W., Pak, D.K., Spero, H.J., 2002. Core top calibration of Mg/Ca in tropical foraminifera: Refining paleotemperature estimation. Geochem. Geophys. Geosyst. 3 (4), 1–29. https://doi.org/10.1029/2001GC000200.
deMenocal, P., Ortiz, J., Guilderson, T., Adkins, J., Sarnthein, M., Baker, L., Yarusinsky, M., 2000a. Abrupt onset and termination of the African Humid Period. Quat. Sci. Rev. 19 (1–5), 347–361. https://doi.org/10.1016/S0277-3791(99)00081-5.
deMenocal, P., Ortiz, J., Guilderson, T., Sarnthein, M., 2000b. Coherent High- and Low-Latitude Climate Variability during the Holocene Warm Period. Science 288, 2198–2202. https://doi.org/10.1126/science.288.5474.2198.
deMenocal, P.B., 2015. End of the African Humid Period. Nat. Geosci. 8, 86–87. https://doi.org/10.1038/ngeo2355.
Doi, T., Tozuka, T., Yamagata, T., 2009. Interannual variability of the Guinea Dome and its possible link with the Atlantic Meridional Mode. Clim. Dyn. 33 (7–8), 985–998. https://doi.org/10.1007/s00382-009-0574-z.
Duggen, S., Croot, P., Schacht, U., Hoffmann, L., 2007. Subduction zone volcanic ash can fertilize the surface ocean and stimulate phytoplankton growth: Evidence from biogeochemical experiments and satellite data. Geophys. Res. Lett. 34 (1), L01612. https://doi.org/10.1029/2006GL027522.
Eglinton, T.I., Eglinton, G., Dupont, L., Sholkovitz, E.R., Montluçon, D., Reddy, C.M., 2002. Composition, age, and provenance of organic matter in NW African dust over the Atlantic Ocean. Geochem. Geophys. Geosyst. 3 (8), 1–27. https://doi.org/10.1029/2001GC000269.
Eisele, S., Reißig, S., Freundt, A., Kutterolf, S., Nürnberg, D., Wang, K.L., Kwasnitschka, T., 2015. Pleistocene to Holocene offshore tephrostratigraphy of highly explosive eruptions from the southwestern Cape Verde Archipelago. Mar. Geol. 369, 233–250. https://doi.org/10.1016/j.margeo.2015.09.006.
Engelstaedter, S., Tegen, I., Washington, R., 2006. North African dust emissions and transport. Earth Sci. Rev. 79 (1–2), 73–100. https://doi.org/10.1016/j.earscirev.2006.06.004.
Ericson, D.B., Wollin, G., 1968. Pleistocene Climates and Chronology in Deep-Sea Sediments: Magnetic reversals give a time scale of 2 million years for a complete Pleistocene with four glaciations. Science 162, 1227–1234. https://doi.org/10.1126/science.162.3859.1227.
Fernández-Carrera, A., Kiko, R., Hauss, H., Hamilton, D.S., Achterberg, E.P., Montoya, J. P., Dengler, M., Brandt, P., Subramaniam, A., 2023. Nitrogen fixation rates in the Guinea Dome and the equatorial upwelling regions in the Atlantic Ocean. Biogeochemistry 166 (3), 191–210. https://doi.org/10.1007/s10533-023-01089-w.
Ferretti, P., Crowhurst, S.J., Naafs, B.D.A., Barbante, C., 2015. The Marine Isotope Stage 19 in the mid-latitude North Atlantic Ocean: astronomical signature and intra-interglacial variability. Quat. Sci. Rev. 108, 95–110. https://doi.org/10.1016/j.quascirev.2014.10.024.
Fischel, A., Seidenkrantz, M.-S., Nürnberg, D., Kučera, M., Kuijpers, A., 2017. Upper water mass variability in the Anegada–Jungfern Passage, NE Caribbean, during the last 11,100 cal. yr. The Holocene 27 (9), 1291–1307. https://doi.org/10.1177/0959683616687378.
Flores, J.-A., Bárcena, M.A., Sierro, F.J., 2000. Ocean-surface and wind dynamics in the Atlantic Ocean off Northwest Africa during the last 140 000 years. Palaeogeogr. Palaeoclimatol. Palaeoecol. 161 (3–4), 459–478. https://doi.org/10.1016/S0031-0182(00)00099-7.
Gabric, A.J., Garcia, L., Van Camp, L., Nykjaer, L., Eifler, W., Schrimpf, W., 1993. Offshore export of shelf production in the Cape Blanc (Mauritania) giant filament as derived from coastal zone color scanner imagery. J. Geophys. Res. Oceans 98 (C3), 4697–4712. https://doi.org/10.1029/92JC01714.
Gaetani, M., Messori, G., Pausata, F.S.R., Tiwari, S., Alvarez Castro, M.C., Zhang, Q., 2024. Mid-Holocene climate at mid-latitudes: assessing the impact of Saharan greening. Clim. Past 20 (8), 1735–1759. https://doi.org/10.5194/cp-20-1735-2024.
García-Reyes, M., Sydeman, W.J., Schoeman, D.S., Rykaczewski, R.R., Black, B.A., Smit, A.J., Bograd, S.J., 2015. Under Pressure: Climate Change, Upwelling, and Eastern Boundary Upwelling Ecosystems. Front. Mar. Sci. 2. https://doi.org/10.3389/fmars.2015.00109.
Gauchery, T., Rovere, M., Pellegrini, C., Asioli, A., Tesi, T., Cattaneo, A., Trincardi, F., 2021. Post-LGM multi-proxy sedimentary record of bottom-current variability and downslope sedimentary processes in a contourite drift of the Gela Basin (Strait of Sicily). Mar. Geol. 439, 106564. https://doi.org/10.1016/j.margeo.2021.106564.
GEBCO Bathymetric Compilation Group, 2021. The GEBCO_2021 Grid - a continuous terrain model of the global oceans and land. 10.5285/C6612CBE-50B3-0CFF-E053-6C86ABC09F8F.
Gläser, G., Wernli, H., Kerkweg, A., Teubler, F., 2015. The transatlantic dust transport from North Africa to the Americas—Its characteristics and source regions. J. Geophys. Res. Atmos. 120 (21). https://doi.org/10.1002/2015JD023792.
Gottschalk, J., Hodell, D.A., Skinner, L.C., Crowhurst, S.J., Jaccard, S.L., Charles, C., 2018. Past Carbonate Preservation Events in the Deep Southeast Atlantic Ocean (Cape Basin) and Their Implications for Atlantic Overturning Dynamics and Marine Carbon Cycling. Paleoceanogr. Paleoclimatol. 33 (6), 643–663. https://doi.org/10.1029/2018PA003353.
Goudie, A.S., Middleton, N.J., 2001. Saharan dust storms: nature and consequences. Earth Sci. Rev. 56 (1–4), 179–204. https://doi.org/10.1016/S0012-8252(01)00067-8.
Govin, A., Holzwarth, U., Heslop, D., Ford Keeling, L., Zabel, M., Mulitza, S., Collins, J. A., Chiessi, C.M., 2012. Distribution of major elements in Atlantic surface sediments (36°N–49°S): Imprint of terrigenous input and continental weathering. Geochem. Geophys. Geosyst. 13 (1), Q01013. https://doi.org/10.1029/2011GC003785.
Gregoire, L.J., Ivanovic, R.F., Maycock, A.C., Valdes, P.J., Stevenson, S., 2018. Holocene lowering of the Laurentide ice sheet affects North Atlantic gyre circulation and climate. Clim. Dyn. 51 (9–10), 3797–3813. https://doi.org/10.1007/s00382-018-4111-9.
Grevemeyer, I., Helffrich, G., Faria, B., Booth-Rea, G., Schnabel, M., Weinrebe, W., 2010. Seismic activity at Cadamosto seamount near Fogo Island, Cape Verdes-formation of a new ocean island? Geophys. J. Int. 180 (2), 552–558. https://doi.org/10.1111/j.1365-246X.2009.04440.x.
Haug, G.H., Hughen, K.A., Sigman, D.M., Peterson, L.C., Röhl, U., 2001a. Southward Migration of the Intertropical Convergence Zone Through the Holocene. Science 293, 1304–1308. https://doi.org/10.1126/science.1059725.
Haug, G.H., Hughen, K.A., Sigman, D.M., Peterson, L.S., Röhl, U., 2001b. Cariaco basin trace metal data (iron, raw data) of ODP Hole 165-1002C. PANGAEA.
Heaton, T.J., Köhler, P., Butzin, M., Bard, E., Reimer, R.W., Austin, W.E.N., Bronk Ramsey, C., Grootes, P.M., Hughen, K.A., Kromer, B., Reimer, P.J., Adkins, J., Burke, A., Cook, M.S., Olsen, J., Skinner, L.C., 2020. Marine20—The Marine Radiocarbon Age Calibration Curve (0–55,000 cal BP). Radiocarbon 62 (4), 779–820. https://doi.org/10.1017/RDC.2020.68.
Henry, L.-A., Frank, N., Hebbeln, D., Wienberg, C., Robinson, L., De Flierdt, T.V., Dahl, M., Douarin, M., Morrison, C.L., Correa, M.L., Rogers, A.D., Ruckelshausen, M., Roberts, J.M., 2014. Global ocean conveyor lowers extinction risk in the deep sea. Deep Sea Res. Part I 88, 8–16. https://doi.org/10.1016/j.dsr.2014.03.004.
Hernández-Guerra, A., Machín, F., Antoranz, A., Cisneros-Aguirre, J., Gordo, C., Marrero-Díaz, A., Martínez, A., Ratsimandresey, A.W., Rodríguez-Santana, A., Sangrá, P., López-Laazen, F., Parrilla, G., Pelegrí, J.L, 2002. Temporal variability of mass transport in the Canary Current. Deep Sea Res. Part II 49 (17), 3415–3426. https://doi.org/10.1016/S0967-0645(02)00092-9.
Hillaire-Marcel, C., De Vernal, A., Bilodeau, G., Weaver, A.J., 2001. Absence of deep-water formation in the Labrador Sea during the last interglacial period. Nature 410, 1073–1077. https://doi.org/10.1038/35074059.
Holloway, M.D., Sime, L.C., Singarayer, J.S., Tindall, J.C., Valdes, P.J., 2016. Reconstructing paleosalinity from $\delta^{18}O$: Coupled model simulations of the Last Glacial Maximum, Last Interglacial and Late Holocene. Quat. Sci. Rev. 131, 350–364. https://doi.org/10.1016/j.quascirev.2015.07.007.
Holm, P.M., Wilson, J.R., Christensen, B.P., Hansen, L., Hansen, S.L., Hein, K.M., Mortensen, A.K., Pedersen, R., Plesner, S., Runge, M.K., 2006. Sampling the Cape Verde Mantle Plume: Evolution of Melt Compositions on Santo Antão, Cape Verde Islands. J. Petrol. 47 (1), 145–189. https://doi.org/10.1093/petrology/egi071.
Hoogakker, B.A.A., Chapman, M.R., McCave, I.N., Hillaire-Marcel, C., Ellison, C.R.W., Hall, I.R., Telford, R.J., 2011. Dynamics of North Atlantic Deep Water masses during the Holocene. Paleoceanography 26 (4), PA4214. https://doi.org/10.1029/2011PA002155.
Hopcroft, P.O., Valdes, P.J., Ingram, W., 2021. Using the Mid-Holocene "Greening" of the Sahara to Narrow Acceptable Ranges on Climate Model Parameters. Geophys. Res. Lett. 48 (6), e2020GL092043. https://doi.org/10.1029/2020GL092043.
Hüls, M., Zahn, R., 2000. Millennial-scale sea surface temperature variability in the western tropical North Atlantic from planktonic foraminiferal census counts. Paleoceanography 15 (6), 659–678. https://doi.org/10.1029/1999PA000462.
Hunt, J.B., Hill, P.G., 2001. Tephrological implications of beam size—sample-size effects in electron microprobe analysis of glass shards. J. Quat. Sci. 16 (2), 105–117. https://doi.org/10.1002/jqs.571.
Hut, G., 1987. Consultants' Group Meeting on Stable Isotope Reference Samples for Geochemical and Hydrological Investigations. IAEA, Vienna, Austria.
Huvenne, V., Orejas, C., Raddatz, J., Pérez, I., 2022. Paleoceanography, in: Orejas, C., Huvenne, V., Sweetman, A.K., Vinha, B., Abella, J.C., Andrade, P., Afonso, A., Antelo, J., Austin-Berry, R., Baltasar, L., Nadito Barbosa, Barnhill, K.A., Barreiro, A., Bettencourt, R., Blanco, S., Buigues, A., Calado, A., Casal, I., De La Torre, J., Dinis, H., Domínguez, I., Domínguez, M., Domínguez, J.I., Evans, S., De Jonge, D., Fairbain, S., Fernández, J.I., Ferradans, M., González-Solís, J., Gori, A., Gunn, V., Hernández, M., Llobet, J., Krazimir Medkov, Menéndez, M., Mocholi, R., Mosquera-Giménez, Á.,

Mouzo, I., O'hobain, E., Palacios, R., Pérez, I., Ponte, C., Prego, T., Raddatz, J., Ramos, B., J. Murray Roberts, Rodríguez, P., Ropert, D., Xoel Salgueiro, Sánchez, M., Simon-Lledó, E., Smith, A., Souto, M., Vélez-Belchí, P. (Eds.), Expedition Report iMirabilis2 Survey. Zenodo, pp. 121–125. 10.5281/ZENODO.6352140.

Itambi, A.C., von Dobeneck, T., Mulitza, S., Bickert, T., Heslop, D., 2009. Millennial-scale northwest African droughts related to Heinrich events and Dansgaard-Oeschger cycles: Evidence in marine sediments from offshore Senegal. Paleoceanography 24 (1), PA1205. https://doi.org/10.1029/2007PA001570.

Jarosewich, E., Nelen, J.A., Norberg, J.A., 1980. Reference Samples for Electron Microprobe Analysis. Geostand. Newslett. 4 (1), 43–47. https://doi.org/10.1111/j.1751-908X.1980.tb00273.x.

Jenkins, W.J., Smethie, W.M., Boyle, E.A., Cutter, G.A., 2015. Water mass analysis for the U.S. GEOTRACES (GA03) North Atlantic sections. Deep Sea Res. Part II 116, 6–20. https://doi.org/10.1016/j.dsr2.2014.11.018.

Johns, W.E., Devana, M., Houk, A., Zou, S., 2021. Moored Observations of the Iceland-Scotland Overflow Plume Along the Eastern Flank of the Reykjanes Ridge. J. Geophys. Res. Oceans 126 (8), e2021JC017524. https://doi.org/10.1029/2021JC017524.

Jullien, E., Grousset, F., Malaizé, B., Duprat, J., Sanchez-Goni, M.F., Eynaud, F., Charlier, K., Schneider, R., Bory, A., Bout, V., Flores, J.A., 2007. Low-latitude "dusty events" vs. high-latitude "icy Heinrich Events. Quat. Res. 68 (3), 379–386. https://doi.org/10.1016/j.yqres.2007.07.007.

Karakaş, G., Nowald, N., Blaas, M., Marchesiello, P., Frickenhaus, S., Schlitzer, R., 2006. High-resolution modeling of sediment erosion and particle transport across the northwest African shelf. J. Geophys. Res. Oceans 111 (C6), C06025. https://doi.org/10.1029/2005JC003296.

Kaufman, D., 2004. Holocene thermal maximum in the western Arctic (0–180°W). Quat. Sci. Rev. 23 (5–6), 529–560. https://doi.org/10.1016/j.quascirev.2003.09.007.

Kaufman, D., McKay, N., Routson, C., Erb, M., Dätwyler, C., Sommer, P.S., Heiri, O., Davis, B., 2020. Holocene global mean surface temperature, a multi-method reconstruction approach. Sci. Data 7 (1), 201. https://doi.org/10.1038/s41597-020-0530-7.

Kogarko, L.N., Sorokhtina, N.V., Zaitsev, V.A., Senin, V.G., 2009. Rare metal mineralization of calcite carbonatites from the Cape Verde Archipelago. Geochem. Int. 47 (6), 531–549. https://doi.org/10.1134/S0016702909060019.

Kröpelin, S., Verschuren, D., Lézine, A.-M., Eggermont, H., Cocquyt, C., Francus, P., Cazet, J.-P., Fagot, M., Rumes, B., Russell, J.M., Darius, F., Conley, D.J., Schuster, M., von Suchodoletz, H., Engstrom, D.R., 2008. Climate-Driven Ecosystem Succession in the Sahara: The Past 6000 Years. Science 320, 765–768. https://doi.org/10.1126/science.1154913.

Kuleshova, L.A., Bashirova, L.D., Matul, A.G., Andersen, N., Ponomarenko, E.P., 2022. Changing sea-surface and deep-water conditions in the southern Cape Verde Basin during the mid-Pleistocene to Holocene. Palaeogeogr. Palaeoclimatol. Palaeoecol. 594, 110921. https://doi.org/10.1016/j.palaeo.2022.110921.

Kuper, R., Kröpelin, S., 2006. Climate-Controlled Holocene Occupation in the Sahara: Motor of Africa's Evolution. Science 313, 803–807. https://doi.org/10.1126/science.1130989.

Kushnir, Y., Robinson, W.A., Chang, P., Robertson, A.W., 2006. The Physical Basis for Predicting Atlantic Sector Seasonal-to-Interannual Climate Variability. J. Clim. 19 (23), 5949–5970. https://doi.org/10.1175/JCLI3943.1.

Kutterolf, S., Freundt, A., Burkert, C., 2011. Eruptive history and magmatic evolution of the 1.9 kyr Plinian dacitic Chiltepe Tephra from Apoyeque volcano in west-central Nicaragua. Bull. Volcanol. 73 (7), 811–831. https://doi.org/10.1007/s00445-011-0457-0.

Kwasnitschka, T., Hansteen, T.H., Ramalho, R.S., Devey, C.W., Klügel, A., Samrock, L.K., Wartho, J.-A., 2024. Geomorphology and Age Constraints of Seamounts in the Cabo Verde Archipelago, and Their Relationship to Island Ages and Geodynamic Evolution. Geochem. Geophys. Geosyst. 25 (3), e2023GC011071. https://doi.org/10.1029/2023GC011071.

Lamy, F., Arz, H.W., Kilian, R., Lange, C.B., Lembke-Jene, L., Wengler, M., Kaiser, J., Baeza-Urrea, O., Hall, I.R., Harada, N., Tiedemann, R., 2015. Glacial reduction and millennial-scale variations in Drake Passage throughflow. Proc. Natl. Acad. Sci. 112 (44), 13496–13501. https://doi.org/10.1073/pnas.1509203112.

Larrasoaña, J.C., Roberts, A.P., Rohling, E.J., 2013. Dynamics of Green Sahara Periods and Their Role in Hominin Evolution. PLoS One 8 (10), e76514. https://doi.org/10.1371/journal.pone.0076514.

Laskar, J., Robutel, P., Joutel, F., Gastineau, M., Correia, A.C.M., Levrard, B., 2004. A long-term numerical solution for the insolation quantities of the Earth. Astron. Astrophys. 428 (1), 261–285. https://doi.org/10.1051/0004-6361:20041335.

Le Maitre, R.W., Streckeisen, A., Zanettin, B., Le Bas, M.J., Bonin, B., Bateman, P. (Eds.), 2002. Igneous Rocks: A Classification and Glossary of Terms, 2nd ed. Cambridge University Press, Cambridge. 10.1017/CBO9780511535581.

Liu, M., Tanhua, T., 2021. Water masses in the Atlantic Ocean: characteristics and distributions. Ocean Sci. 17 (2), 463–486. https://doi.org/10.5194/os-17-463-2021.

Liu, X., Luo, Y., Boudreau, B.P., 2022. Effects of Deep Circulation on $CaCO_3$ Dissolution and Accumulation in the Southwestern Atlantic Ocean. Geophys. Res. Lett. 49 (2), e2021GL095020. https://doi.org/10.1029/2021GL095020.

Liu, X., Rendle-Bühring, R., Kuhlmann, H., Li, A., 2017. Two phases of the Holocene East African Humid Period: Inferred from a high-resolution geochemical record off Tanzania. Earth Planet. Sci. Lett. 460, 123–134. https://doi.org/10.1016/j.epsl.2016.12.016.

Liu, Z., Brady, E., Lynch-Stieglitz, J., 2003. Global ocean response to orbital forcing in the Holocene. Paleoceanography 18 (2), 1041. https://doi.org/10.1029/2002PA000819.

Lohmann, K., Mignot, J., Langehaug, H.R., Jungclaus, J.H., Matei, D., Otterå, O.H., Gao, Y.Q., Mjell, T.L., Ninnemann, U.S., Kleiven, H.F., 2015. Using simulations of the last millennium to understand climate variability seen in palaeo-observations: similar variation of Iceland–Scotland overflow strength and Atlantic Multidecadal Oscillation. Clim. Past 11 (2), 203–216. https://doi.org/10.5194/cp-11-203-2015.

Mackensen, A., Hubberten, H.-W., Bickert, T., Fischer, G., Fütterer, D.K., 1993. The $\delta^{13}C$ in benthic foraminiferal tests of *Fontbotia wuellerstorfi* (Schwager) Relative to the $\delta^{13}C$ of dissolved inorganic carbon in Southern Ocean Deep Water: Implications for glacial ocean circulation models. Paleoceanography 8 (5), 587–610. https://doi.org/10.1029/93PA01291.

Madeira, J., Mata, J., Mourão, C., Brum Da Silveira, A., Martins, S., Ramalho, R., Hoffmann, D.L., 2010. Volcano-stratigraphic and structural evolution of Brava Island (Cape Verde) based on $^{40}Ar/^{39}Ar$, U–Th and field constraints. J. Volcanol. Geoth. Res. 196 (3–4), 219–235. https://doi.org/10.1016/j.jvolgeores.2010.07.010.

Magny, M., De Beaulieu, J.-L., Drescher-Schneider, R., Vannière, B., Walter-Simonnet, A.-V., Miras, Y., Millet, L., Bossuet, G., Peyron, O., Brugiapaglia, E., Leroux, A., 2007. Holocene climate changes in the central Mediterranean as recorded by lake-level fluctuations at Lake Accesa (Tuscany, Italy). Quat. Sci. Rev. 26 (13–14), 1736–1758. https://doi.org/10.1016/j.quascirev.2007.04.014.

Manighetti, B., McCave, I.N., Maslin, M., Shackleton, N.J., 1995. Chronology for climate change: Developing age models for the biogeochemical ocean flux study cores. Paleoceanography 10 (3), 513–525. https://doi.org/10.1029/94PA2.

Martin-Puertas, C., Matthes, K., Brauer, A., Muscheler, R., Hansen, F., Petrick, C., Aldahan, A., Possnert, G., Van Geel, B., 2012. Regional atmospheric circulation shifts induced by a grand solar minimum. Nat. Geosci. 5, 397–401. https://doi.org/10.1038/ngeo1460.

Matsuzaki, K.M.R., Eynaud, F., Malaizé, B., Grousset, F.E., Tisserand, A., Rossignol, L., Charlier, K., Jullien, E., 2011. Paleoceanography of the Mauritanian margin during the last two climatic cycles: From planktonic foraminifera to African climate dynamics. Mar. Micropaleontol. 79 (3–4), 67–79. https://doi.org/10.1016/j.marmicro.2011.01.004.

Mayewski, P.A., Rohling, E.E., Curt Stager, J., Karlén, W., Maasch, K.A., Meeker, L.D., Meyerson, E.A., Gasse, F., Van Kreveld, S., Holmgren, K., Lee-Thorp, J., Rosqvist, G., Rack, F., Staubwasser, M., Schneider, R.R., Steig, E.J., 2004. Holocene climate variability. Quat. Res. 62 (3), 243–255. https://doi.org/10.1016/j.yqres.2004.07.001.

Mazeika, P.A., 1967. Thermal Domes in the Eastern Tropical Atlantic Ocean. Limnol. Oceanogr. 12 (3), 537–539. https://doi.org/10.4319/lo.1967.12.3.0537.

McCave, I.N., Thornalley, D.J.R., Hall, I.R., 2017. Relation of sortable silt grain-size to deep-sea current speeds: Calibration of the 'Mud Current Meter. Deep Sea Res. Part I 127, 1–12. https://doi.org/10.1016/j.dsr.2017.07.003.

McGregor, H.V., Dima, M., Fischer, H.W., Mulitza, S., 2007. Rapid 20th-Century Increase in Coastal Upwelling off Northwest Africa. Science 315, 637–639. https://doi.org/10.1126/science.1134839.

McIntyre, A., Molfino, B., 1996. Forcing of Atlantic Equatorial and Subpolar Millennial Cycles by Precession. Science 274, 1867–1870. https://doi.org/10.1126/science.274.5294.1867.

McIntyre, A., Ruddiman, W.F., Karlin, K., Mix, A.C., 1989. Surface water response of the equatorial Atlantic Ocean to orbital forcing. Paleoceanography 4 (1), 19–55. https://doi.org/10.1029/PA004i001p00019.

McKay, C.L., Filipsson, H.L., Romero, O.E., Stuut, J.B.W., Donner, B., 2014. Pelagic–benthic coupling within an upwelling system of the subtropical northeast Atlantic over the last 35 ka BP. Quat. Sci. Rev. 106, 299–315. https://doi.org/10.1016/j.quascirev.2014.04.027.

Meggers, H., Freudenthal, T., Nave, S., Targarona, J., Abrantes, F., Helmke, P., 2002. Assessment of geochemical and micropaleontological sedimentary parameters as proxies of surface water properties in the Canary Islands region. Deep Sea Res. Part II 49 (17), 3631–3654. https://doi.org/10.1016/S0967-0645(02)00103-0.

Mekik, F., 2014. Radiocarbon dating of planktonic foraminifer shells: A cautionary tale. Paleoceanography 29 (1), 13–29. https://doi.org/10.1002/2013PA002532.

Metcalf, W.G., Heezen, B.C., Stalcup, M.C., 1964. The sill depth of the Mid-Atlantic Ridge in the equatorial region. Deep-Sea Res. Oceanogr. Abstr. 11 (1), 1–10. https://doi.org/10.1016/0011-7471(64)91078-2.

Mirzaloo, M., Nürnberg, D., Kienast, M., Van Der Lubbe, H.J.L., 2019. Synchronous Changes in Sediment Transport and Provenance at the Iceland-Faroe Ridge Linked to Millennial Climate Variability From 55 to 6 ka BP. Geochem. Geophys. Geosyst. 20 (8), 4184–4201. https://doi.org/10.1029/2019GC008298.

Mjell, T.L., Ninnemann, U.S., Kleiven, H.F., Hall, I.R., 2016. Multidecadal changes in Iceland Scotland Overflow Water vigor over the last 600 years and its relationship to climate. Geophys. Res. Lett. 43 (5), 2111–2117. https://doi.org/10.1002/2016GL068227.

Moffa-Sánchez, P., Hall, I.R., 2017. North Atlantic variability and its links to European climate over the last 3000 years. Nat. Commun. 8 (1), 1726. https://doi.org/10.1038/s41467-017-01884-8.

Montelli, R., Nolet, G., Dahlen, F.A., Masters, G., Engdahl, E.R., Hung, S.-H., 2004. Finite-Frequency Tomography Reveals a Variety of Plumes in the Mantle. Science 303, 338–343. https://doi.org/10.1126/science.1092485.

Mosquera Giménez, Á., Vélez-Belchí, P., Rodríguez, P., Mouzo, I., 2022. Physical oceanography off Cabo Verde, in: Orejas, C., Huvenne, V., Sweetman, A.K., Vinha, B., Abella, J.C., Andrade, P., Afonso, A., Antelo, J., Austin-Berry, R., Baltasar, L., Nadito Barbosa, Barnhill, K.A., Barreiro, A., Bettencourt, R., Blanco, S., Buigues, A., Calado, A., Casal, I., De La Torre, J., Dinis, H., Domínguez, I., Domínguez, M., Domínguez, J.I., Evans, S., De Jonge, D., Fairbain, S., Fernández, J.I., Ferradans, M., González-Solís, J., Gori, A., Gunn, V., Hernández, M., Llobet, J., Krazimir Medkov, Menéndez, M., Mocholi, R., Mosquera-Giménez, Á., Mouzo, I., O'hobain, E., Palacios, R., Pérez, I., Ponte, C., Prego, T., Raddatz, J., Ramos, B., J. Murray Roberts, Rodríguez, Pablo, Ropert, D., Xoel Salgueiro, Sánchez, M., Simon-Lledó, E., Smith,

A., Souto, M., Vélez-Belchí, P. (Eds.), Expedition Report iMirabilis2 Survey. Zenodo, pp. 62–75. 10.5281/ZENODO.6352140.
Moy, C.M., Seltzer, G.O., Rodbell, D.T., Anderson, D.M., 2002. Variability of El Niño/Southern Oscillation activity at millennial timescales during the Holocene epoch. Nature 420, 162–165. https://doi.org/10.1038/nature01194.
Mulitza, S., Prange, M., Stuut, J.-B., Zabel, M., von Dobeneck, T., Itambi, A.C., Nizou, J., Schulz, M., Wefer, G., 2008. Sahel megadroughts triggered by glacial slowdowns of Atlantic meridional overturning. Paleoceanography 23 (4), PA4206. https://doi.org/10.1029/2008PA001637.
Nakanishi, T., Tachibana, Y., Ando, Y., 2021. Possible semi-circumglobal teleconnection across Eurasia driven by deep convection over the Sahel. Clim. Dyn. 57 (7–8), 2287–2299. https://doi.org/10.1007/s00382-021-05804-x.
Nascimento, R.A., Venancio, I.M., Chiessi, C.M., Ballalai, J.M., Kuhnert, H., Johnstone, H., Santos, T.P., Prange, M., Govin, A., Crivellari, S., Mulitza, S., Albuquerque, A.L.S., 2021. Tropical Atlantic stratification response to late Quaternary precessional forcing. Earth Planet. Sci. Lett. 568, 117030. https://doi.org/10.1016/j.epsl.2021.117030.
Nürnberg, D., Riff, T., Bahr, A., Karas, C., Meier, K.J.F., Lippold, J., 2020. Stable isotopes and Mg/Ca ratios of Globorotalia truncatulinoides from sediment core M78/1_235-1. PANGAEA.
Nürnberg, D., Ziegler, M., Karas, C., Tiedemann, R., Schmidt, M.W., 2008. Interacting Loop Current variability and Mississippi River discharge over the past 400 kyr. Earth Planet. Sci. Lett. 272 (1–2), 278–289. https://doi.org/10.1016/j.epsl.2008.04.051.
O'Brien, C.L., Spooner, P.T., Wharton, J.H., Papachristopoulou, E., Dutton, N., Fairman, D., Garratt, R., Li, T., Pallottino, F., Stringer, F., Thornalley, D.J.R., 2021. Exceptional 20th Century Shifts in Deep-Sea Ecosystems Are Spatially Heterogeneous and Associated With Local Surface Ocean Variability. Front. Mar. Sci. 8, 663009. https://doi.org/10.3389/fmars.2021.663009.
Ohnemus, D.C., Lam, P.J., 2015. Cycling of lithogenic marine particles in the US GEOTRACES North Atlantic transect. Deep Sea Res. Part II 116, 283–302. https://doi.org/10.1016/j.dsr2.2014.11.019.
Oppo, D.W., McManus, J.F., Cullen, J.L., 2003. Deepwater variability in the Holocene epoch. Nature 422, 277. https://doi.org/10.1038/422277b.
Orejas, C., Huvenne, V., Sweetman, A.K., Vinha, B., Abella, J.C., Andrade, P., Afonso, A., Antelo, J., Austin-Berry, R., Baltasar, L., Barbosa, N., Barnhill, K.A., Barreiro, A., Bettencourt, R., Blanco, S., Buigues, A., Calado, A., Casal, I., De La Torre, J., Dinis, H., Domínguez, I., Domínguez, M., Domínguez, J.I., Evans, S., De Jonge, D., Fairbain, S., Fernández, J.I., Ferradans, M., González-Solís, J., Gori, A., Gunn, V., Hernández, M., Llobet, J., Medkov, K., Menéndez, M., Mocholi, R., Mosquera-Giménez, Á., Mouzo, I., O'hobain, E., Palacios, R., Pérez, I., Ponte, C., Prego, T., Raddatz, J., Ramos, B., J. Murray Roberts, Rodríguez, P., Ropert, D., Xoel Salgueiro, Sánchez, M., Simon-Lledó, E., Smith, A., Souto, M., Vélez-Belchí, P., 2022. Expedition report iMirabilis2 survey. Zenodo. https://doi.org/10.5281/ZENODO.6352140.
Pauly, D., Christensen, V., 1995. Primary production required to sustain global fisheries. Nature 374, 255–257. https://doi.org/10.1038/374255a0.
Pausata, F.S.R., Gaetani, M., Messori, G., Berg, A., Maia De Souza, D., Sage, R.F., deMenocal, P.B., 2020. The Greening of the Sahara: Past Changes and Future Implications. One Earth 2 (3), 235–250. https://doi.org/10.1016/j.oneear.2020.03.002.
Pausata, F.S.R., Messori, G., Zhang, Q., 2016. Impacts of dust reduction on the northward expansion of the African monsoon during the Green Sahara period. Earth Planet. Sci. Lett. 434, 298–307. https://doi.org/10.1016/j.epsl.2015.11.049.
Pelegrí, J.L., Arístegui, J., Cana, L., González-Dávila, M., Hernández-Guerra, A., Hernández-León, S., Marrero-Díaz, A., Montero, M.F., Sangrà, P., Santana-Casiano, M., 2005. Coupling between the open ocean and the coastal upwelling region off northwest Africa: water recirculation and offshore pumping of organic matter. J. Mar. Syst. 54 (1–4), 3–37. https://doi.org/10.1016/j.jmarsys.2004.07.003.
Pelegrí, J.L., Peña-Izquierdo, J., Machín, F., Meiners, C., Presas-Navarro, C., 2017. Oceanography of the Cape Verde Basin and Mauritanian Slope Waters. In: Ramos, A., Ramil, F., Sanz, J.L. (Eds.), Deep-Sea Ecosystems Off Mauritania. Springer, Netherlands, Dordrecht, pp. 119–153. https://doi.org/10.1007/978-94-024-1023-5_3.
Pérez-Rodríguez, I., Nürnberg, D., Schindlbeck-Belo, J., Wharton, J., Hansteen, T.H., Huvenne, V.A.I., Thornalley, D.J.R., Mosquera Giménez, Á., Kutterolf, S., Barnhill, K.A., Orejas, C., 2024a. XRF-scanning elemental data and core descriptions from sediment cores obtained southwest off the Cabo Verde archipelago. PANGAEA.
Pérez-Rodríguez, I., Nürnberg, D., Schindlbeck-Belo, J., Wharton, J., Hansteen, T.H., Huvenne, V.A.I., Thornalley, D.J.R., Mosquera Giménez, Á., Kutterolf, S., Barnhill, K.A., Orejas, C., 2024b. Microfossil census counts from a Holocene sediment core obtained southwest off the Cabo Verde archipelago (MUC5). PANGAEA.
Pérez-Rodríguez, I., Nürnberg, D., Schindlbeck-Belo, J., Wharton, J., Hansteen, T.H., Huvenne, V.A.I., Thornalley, D.J.R., Mosquera Giménez, Á., Kutterolf, S., Barnhill, K.A., Orejas, C., 2024c. Stable isotopes (δ13C and δ18O) and Mg/Ca-based temperatures of Globigerinoides ruber albus from a Holocene sediment core southwest off the Cabo Verde archipelago (MUC5). PANGAEA.
Pérez-Rodríguez, I., Nürnberg, D., Schindlbeck-Belo, J., Wharton, J., Hansteen, T.H., Huvenne, V.A.I., Thornalley, D.J.R., Mosquera Giménez, Á., Kutterolf, S., Barnhill, K.A., Orejas, C., 2024d. Stable isotopes (δ13C and δ18O) and Mg/Ca-based temperatures of Globorotalia truncatulinoides from a Holocene sediment core southwest off the Cabo Verde archipelago (MUC5). PANGAEA.
Pérez-Rodríguez, I., Nürnberg, D., Schindlbeck-Belo, J., Wharton, J., Hansteen, T.H., Huvenne, V.A.I., Thornalley, D.J.R., Mosquera Giménez, Á., Kutterolf, S., Barnhill, K.A., Orejas, C., 2024e. Stable isotopes (δ13C and δ18O) of Cibicidoides wuellerstorfi from a Holocene sediment core southwest off the Cabo Verde archipelago (MUC5). PANGAEA.
Pierre, C., Vangriesheim, A., Laube-Lenfant, E., 1994. Variability of water masses and of organic production-regeneration systems as related to eutrophic, mesotropic and oligotrophic conditions in the northeast Atlantic Ocean. J. Mar. Syst. 5 (2), 159–170. https://doi.org/10.1016/0924-7963(94)90029-9.
Pim, J., Peirce, C., Watts, A.B., Grevemeyer, I., Krabbenhoeft, A., 2008. Crustal structure and origin of the Cape Verde Rise. Earth Planet. Sci. Lett. 272 (1–2), 422–428. https://doi.org/10.1016/j.epsl.2008.05.012.
Prospero, J.M., Ginoux, P., Torres, O., Nicholson, S.E., Gill, T.E., 2002. Environmental Characterization of Global sources of atmospheric soil dust derived from the NIMBUS-7 TOMS absorbing aerosol product. Rev. Geophys. 40 (1). https://doi.org/10.1029/2000RG000095.
Railsback, L.B., Liang, F., Brook, G.A., Voarintsoa, N.R.G., Sletten, H.R., Marais, E., Hardt, B., Cheng, H., Edwards, R.L., 2018. The timing, two-pulsed nature, and variable climatic expression of the 4.2 ka event: A review and new high-resolution stalagmite data from Namibia. Quat. Sci. Rev. 186, 78–90. https://doi.org/10.1016/j.quascirev.2018.02.015.
Ramalho, R.A.S., 2011. Building the Cape Verde Islands. Springer, Berlin Heidelberg, Berlin, Heidelberg. https://doi.org/10.1007/978-3-642-19103-9.
Reagan, J.R., Boyer, T.P., García, H.P., Locarnini, H.P., Baranova, O.K., Bouchard, C., Cross, S.L., Mishonov, A.V., Paver, C.R., Seidov, D., Wang, Z., Dukhovskoy, D., 2024. World Ocean Atlas 2023. NOAA National Centers for Environmental Information. Dataset: NCEI Accession 0270533. https://www.ncei.noaa.gov/access/metadata/landing-page/bin/iso?id=gov.noaa.nodc:0270533.
Regenberg, M., Regenberg, A., Garbe-Schönberg, D., Lea, D.W., 2014. Global dissolution effects on planktonic foraminiferal Mg/Ca ratios controlled by the calcite-saturation state of bottom waters. Paleoceanography 29 (3), 127–142. https://doi.org/10.1002/2013PA002492.
Reißig, S., Nürnberg, D., Bahr, A., Poggemann, D.-W., Hoffmann, J., 2019. Southward Displacement of the North Atlantic Subtropical Gyre Circulation System During North Atlantic Cold Spells. Paleoceanogr. Paleoclimatol. 34 (5), 866–885. https://doi.org/10.1029/2018PA003376.
Repschläger, J., Garbe-Schönberg, D., Weinelt, M., Schneider, R., 2017. Holocene evolution of the North Atlantic subsurface transport. Clim. Past 13 (4), 333–344. https://doi.org/10.5194/cp-13-333-2017.
Repschläger, J., Weinelt, M., Kinkel, H., Andersen, N., Garbe-Schönberg, D., Schwab, C., 2015. Response of the subtropical North Atlantic surface hydrography on deglacial and Holocene AMOC changes. Paleoceanography 30 (5), 456–476. https://doi.org/10.1002/2014PA002637.
Repschläger, J., Zhao, N., Rand, D., Lisiecki, L., Muglia, J., Mulitza, S., Schmittner, A., Cartapanis, O., Bauch, H.A., Schiebel, R., Haug, G.H., 2021. Active North Atlantic deepwater formation during Heinrich Stadial 1. Quat. Sci. Rev. 270 (D2), 107145. https://doi.org/10.1016/j.quascirev.2021.107145.
Ridley, D.A., Heald, C.L., Ford, B., 2012. North African dust export and deposition: A satellite and model perspective. J. Geophys. Res. Atmos. 117 (D2), D02202. https://doi.org/10.1029/2011JD016794.
Rodríguez, S., Riera, R., Fonteneau, A., Alonso-Pérez, S., López-Darias, J., 2023. African desert dust influences migrations and fisheries of the Atlantic skipjack-tuna. Atmos. Environ. 312, 120022. https://doi.org/10.1016/j.atmosenv.2023.120022.
Rodríguez-Fonseca, B., Mohino, E., Mechoso, C.R., Caminade, C., Biasutti, M., Gaetani, M., Garcia-Serrano, J., Vizy, E.K., Cook, K., Xue, Y., Polo, I., Losada, T., Druyan, L., Fontaine, B., Bader, J., Doblas-Reyes, F.J., Goddard, L., Janicot, S., Arribas, A., Lau, W., Colman, A., Vellinga, M., Rowell, D.P., Kucharski, F., Voldoire, A., 2015. Variability and Predictability of West African Droughts: A Review on the Role of Sea Surface Temperature Anomalies. J. Clim. 28 (10), 4034–4060. https://doi.org/10.1175/JCLI-D-14-00130.1.
Rodríguez-Navarro, C., Di Lorenzo, F., Elert, K., 2018. Mineralogy and physicochemical features of Saharan dust wet deposited in the Iberian Peninsula during an extreme red rain event. Atmos. Chem. Phys. 18 (13), 10089–10122. https://doi.org/10.5194/acp-18-10089-2018.
Romero, O.E., Kim, J., Donner, B., 2008a. Submillennial-to-millennial variability of diatom production off Mauritania, NW Africa, during the last glacial cycle. Paleoceanography 23 (3), PA3218. https://doi.org/10.1029/2008PA001601.
Romero, O.E., Kim, J.-H., Donner, B., 2008b. Diatoms, opal, total organic carbon, calcium carbonate and sea surface temperature of sediment core GeoB7926-2. PANGAEA.
Rossignol, L., 2022. Planktonic foraminifera counts of sediment core MD95-2042 off the Iberian margin for the past 60 ka. PANGAEA.
Rothwell, R.G., Hoogakker, B., Thomson, J., Croudace, I.W., Frenz, M., 2006. Turbidite emplacement on the southern Balearic Abyssal Plain (western Mediterranean Sea) during Marine Isotope Stages 1–3: an application of ITRAX XRF scanning of sediment cores to lithostratigraphic analysis. Geol. Soc. Lond. Spec. Publ. 267 (1), 79–98. https://doi.org/10.1144/GSL.SP.2006.267.01.06.
Rowell, D.P., 2001. Teleconnections between the tropical Pacific and the Sahel. Q. J. R. Meteorolog. Soc. 127 (575), 1683–1706. https://doi.org/10.1002/qj.49712757512.
Sarnthein, M., Tetzlaff, G., Koopmann, B., Wolter, K., Pflaumann, U., 1981. Glacial and interglacial wind regimes over the eastern subtropical Atlantic and North-West Africa. Nature 293, 193–196. https://doi.org/10.1038/293193a0.
Sarre, A., Demarcq, H., Keenlyside, N., Krakstad, J.-O., El Ayoubi, S., Jeyid, A.M., Faye, S., Mbaye, A., Sidibeh, M., Brehmer, P., 2024. Climate change impacts on small pelagic fish distribution in Northwest Africa: trends, shifts, and risk for food security. Sci. Rep. 14 (1), 12684. https://doi.org/10.1038/s41598-024-61734-8.
Schlitzer, R., Mieruch-Schnülle, S., 2024. webODV Explore. Alfred Wegener Institute, Bremerhaven https://explore.webodv.awi.de (accessed 7 May 2025.

Schmidt, G.A., 1999. Forward modeling of carbonate proxy data from planktonic foraminifera using oxygen isotope tracers in a global ocean model. Paleoceanography 14 (4), 482–497. https://doi.org/10.1029/1999PA900025.
Schmidt, G.A., Bigg, G.R., Rohling, E.J., 1999. Global Seawater Oxygen-18 Database - v1.22. https://data.giss.nasa.gov/o18data/ (accessed 9 May 2025).
Schmidt, M.W., Chang, P., Hertzberg, J.E., Them, T.R., Ji, L., Otto-Bliesner, B.L., 2012. Impact of abrupt deglacial climate change on tropical Atlantic subsurface temperatures. Proc. Natl. Acad. Sci. 109 (36), 14348–14352. https://doi.org/10.1073/pnas.1207806109.
Schmittner, A., Bostock, H.C., Cartapanis, O., Curry, W.B., Filipsson, H.L., Galbraith, E. D., Gottschalk, J., Herguera, J.C., Hoogakker, B., Jaccard, S.L., Lisiecki, L.E., Lund, D.C., Martínez-Méndez, G., Lynch-Stieglitz, J., Mackensen, A., Michel, E., Mix, A.C., Oppo, D.W., Peterson, C.D., Repschläger, J., Sikes, E.L., Spero, H.J., Waelbroeck, C., 2017. Calibration of the carbon isotope composition (δ^{13} C) of benthic foraminifera. Paleoceanography 32 (6), 512–530. https://doi.org/10.1002/2016PA003072.
Schneider, R.R., Price, B., Müller, P.J., Kroon, D., Alexander, I., 1997. Monsoon related variations in Zaire (Congo) sediment load and influence of fluvial silicate supply on marine productivity in the east equatorial Atlantic during the last 200,000 years. Paleoceanography 12 (3), 463–481. https://doi.org/10.1029/96PA03640.
Sexton, P.F., Norris, R.D., 2011. High latitude regulation of low latitude thermocline ventilation and planktic foraminifer populations across glacial–interglacial cycles. Earth Planet. Sci. Lett. 311 (1–2), 69–81. https://doi.org/10.1016/j.epsl.2011.08.044.
Skonieczny, C., Paillou, P., Bory, A., Bayon, G., Biscara, L., Crosta, X., Eynaud, F., Malaizé, B., Revel, M., Aleman, N., Barusseau, J.-P., Vernet, R., Lopez, S., Grousset, F., 2015. African humid periods triggered the reactivation of a large river system in Western Sahara. Nat. Commun. 6 (1), 8751. https://doi.org/10.1038/ncomms9751.
Stainforth, R.M., Lamb, J.L., Luterbacher, H., Beard, J.H., Jeffords, R.M., 1975. Cenozoic planktonic foraminiferal zonation and characteristics of index forms. University of Kansas Paleontological Contributions, Articles 62. https://doi.org/10.2307/1484621.
Steph, S., Regenberg, M., Tiedemann, R., Mulitza, S., Nürnberg, D., 2009. Stable isotopes of planktonic foraminifera from tropical Atlantic/Caribbean core-tops: Implications for reconstructing upper ocean stratification. Mar. Micropaleontol. 71 (1–2), 1–19. https://doi.org/10.1016/j.marmicro.2008.12.004.
Stuiver, M., Polach, H.A., 1977. Discussion Reporting of ^{14}C Data. Radiocarbon 19 (3), 355–363. https://doi.org/10.1017/S0033822200003672.
Stuut, J.-B., Zabel, M., Ratmeyer, V., Helmke, P., Schefuß, E., Lavik, G., Schneider, R., 2005. Provenance of present-day eolian dust collected off NW Africa. J. Geophys. Res. Atmos. 110 (D4), D04202. https://doi.org/10.1029/2004JD005161.
Swann, A.L.S., Fung, I.Y., Liu, Y., Chiang, J.C.H., 2014. Remote Vegetation Feedbacks and the Mid-Holocene Green Sahara. J. Clim. 27 (13), 4857–4870. https://doi.org/10.1175/JCLI-D-13-00690.1.
Swap, R., Ulanski, S., Cobbett, M., Garstang, M., 1996. Temporal and spatial characteristics of Saharan dust outbreaks. J. Geophys. Res. Atmos. 101 (D2), 4205–4220. https://doi.org/10.1029/95JD03236.
Talley, L.D., 2011. Descriptive Physical Oceanography. Elsevier Science, Burlington. https://doi.org/10.1016/C2009-0-24322-4.
Tanré, D., Bréon, F.M., Deuzé, J.L., Dubovik, O., Ducos, F., François, P., Goloub, P., Herman, M., Lifermann, A., Waquet, F., 2011. Remote sensing of aerosols by using polarized, directional and spectral measurements within the A-Train: the PARASOL mission. Atmos. Meas. Tech. 4 (7), 1383–1395. https://doi.org/10.5194/amt-4-1383-2011.
Telford, R.J., Li, C., Kučera, M., 2013. Mismatch between the depth habitat of planktonic foraminifera and the calibration depth of SST transfer functions may bias reconstructions. Clim. Past 9 (2), 859–870. https://doi.org/10.5194/cp-9-859-2013.
Thiede, J., 1975. Distribution of foraminifera in surface waters of a coastal upwelling area. Nature 253, 712–714. https://doi.org/10.1038/253712a0.
Thompson, L.G., Mosley-Thompson, E., Davis, M.E., Henderson, K.A., Brecher, H.H., Zagorodnov, V.S., Mashiotta, T.A., Lin, P.-N., Mikhalenko, V.N., Hardy, D.R., Beer, J., 2002. Kilimanjaro Ice Core Records: Evidence of Holocene Climate Change in Tropical Africa. Science 298, 589–593. https://doi.org/10.1126/science.1073198.
Thornalley, D.J.R., Blaschek, M., Davies, F.J., Praetorius, S., Oppo, D.W., McManus, J.F., Hall, I.R., Kleiven, H., Renssen, H., McCave, I.N., 2013. Long-term variations in Iceland–Scotland overflow strength during the Holocene. Clim. Past 9 (5), 2073–2084. https://doi.org/10.5194/cp-9-2073-2013.
Thornalley, D.J.R., Elderfield, H., McCave, I.N., 2010. Intermediate and deep water paleoceanography of the northern North Atlantic over the past 21,000 years. Paleoceanography 25 (1), PA1211. https://doi.org/10.1029/2009PA001833.
Thornalley, D.J.R., Elderfield, H., McCave, I.N., 2009. Holocene oscillations in temperature and salinity of the surface subpolar North Atlantic. Nature 457, 711–714. https://doi.org/10.1038/nature07717.
Tierney, J.E., Pausata, F.S.R., deMenocal, P.B., 2017. Rainfall regimes of the Green Sahara. Sci. Adv. 3 (1), e1601503. https://doi.org/10.1126/sciadv.1601503.
Tisserand, A., Malaizé, B., Jullien, E., Zaragosi, S., Charlier, K., Grousset, F., 2009. African monsoon enhancement during the penultimate glacial period (MIS 6.5 ~ 170 ka) and its atmospheric impact. Paleoceanography 24 (2), PA2220. https://doi.org/10.1029/2008PA001630.
Tolderlund, D.S., Bé, A.W.H., 1971. Seasonal Distribution of Planktonic Foraminifera in the Western North Atlantic. Micropaleontology 17 (3), 297. https://doi.org/10.2307/1485143.
Valdés, L., Déniz-González, I., 2015. Oceanographic and biological features in the Canary Current Large Marine Ecosystem, IOC-UNESCO, IOC Technical Series 115. Paris.
Venancio, I.M., Mulitza, S., Govin, A., Santos, T.P., Lessa, D.O., Albuquerque, A.L.S., Chiessi, C.M., Tiedemann, R., Vahlenkamp, M., Bickert, T., Schulz, M., 2018. Millennial- to Orbital-Scale Responses of Western Equatorial Atlantic Thermocline Depth to Changes in the Trade Wind System Since the Last Interglacial. Paleoceanogr. Paleoclimatol. 33 (12), 1490–1507. https://doi.org/10.1029/2018PA003437.
Walker, M., Head, M.J., Lowe, J., Berkelhammer, M., BjÖrck, S., Cheng, H., Cwynar, L.C., Fisher, D., Gkinis, V., Long, A., Newnham, R., Rasmussen, S.O., Weiss, H., 2019. Subdividing the Holocene Series/Epoch: formalization of stages/ages and subseries/subepochs, and designation of GSSPs and auxiliary stratotypes. J. Quat. Sci. 34 (3), 173–186. https://doi.org/10.1002/jqs.3097.
Wang, L., 2000. Isotopic signals in two morphotypes of *Globigerinoides* ruber (white) from the South China Sea: implications for monsoon climate change during the last glacial cycle. Palaeogeogr. Palaeoclimatol. Palaeoecol. 161 (3–4), 381–394. https://doi.org/10.1016/S0031-0182(00)00094-8.
Wanner, H., Solomina, O., Grosjean, M., Ritz, S.P., Jetel, M., 2011. Structure and origin of Holocene cold events. Quat. Sci. Rev. 30 (21–22), 3109–3123. https://doi.org/10.1016/j.quascirev.2011.07.010.
Weirauch, D., Billups, K., Martin, P., 2008. Evolution of millennial-scale climate variability during the mid-Pleistocene. Paleoceanography 23 (3), PA3216. https://doi.org/10.1029/2007PA001584.
Weldeab, S., Lea, D.W., Schneider, R.R., Andersen, N., 2007. Centennial scale climate instabilities in a wet early Holocene West African monsoon. Geophys. Res. Lett. 34 (24), L24702. https://doi.org/10.1029/2007GL031898.
Weldeab, S., Schneider, R.R., Kölling, M., Wefer, G., 2005. Holocene African droughts relate to eastern equatorial Atlantic cooling. Geology 33 (12), 981. https://doi.org/10.1130/G21874.1.
Weltje, G.J., Tjallingii, R., 2008. Calibration of XRF core scanners for quantitative geochemical logging of sediment cores: Theory and application. Earth Planet. Sci. Lett. 274 (3–4), 423–438. https://doi.org/10.1016/j.epsl.2008.07.054.
Wolff, T., Mulitza, S., Rühlemann, C., Wefer, G., 1999. Response of the tropical Atlantic thermocline to Late Quaternary Trade Wind changes. Paleoceanography 14 (3), 374–383. https://doi.org/10.1029/1999PA900011.
Wu, L., Wilson, D.J., Wang, R., Yin, X., Chen, Z., Xiao, W., Huang, M., 2020. Evaluating Zr/Rb Ratio From XRF Scanning as an Indicator of Grain-Size Variations of Glaciomarine Sediments in the Southern Ocean. Geochem. Geophys. Geosyst. 21 (11), e2020GC009350. https://doi.org/10.1029/2020GC009350.
Yamoula, D., Balogun, I.A., Sow, B.A., 2025. Characterization of Northwest African Coastal Upwelling Systems, EGUsphere [preprint]. 10.5194/egusphere-2024-4175.
Yu, H., Chin, M., Yuan, T., Bian, H., Remer, L.A., Prospero, J.M., Omar, A., Winker, D., Yang, Y., Zhang, Y., Zhang, Z., Zhao, C., 2015. The fertilizing role of African dust in the Amazon rainforest: A first multiyear assessment based on data from Cloud-Aerosol Lidar and Infrared Pathfinder Satellite Observations. Geophys. Res. Lett. 42 (6), 1984–1991. https://doi.org/10.1002/2015GL063040.
Yu, H., Tan, Q., Chin, M., Remer, L.A., Kahn, R.A., Bian, H., Kim, D., Zhang, Z., Yuan, T., Omar, A.H., Winker, D.M., Levy, R.C., Kalashnikova, O., Crepeau, L., Capelle, V., Chédin, A., 2019. Estimates of African Dust Deposition Along the Trans-Atlantic Transit Using the Decadelong Record of Aerosol Measurements from CALIOP, MODIS, MISR, and IASI. J. Geophys. Res. Atmos. 124 (14), 7975–7996. https://doi.org/10.1029/2019JD030574.
Zarriess, M., Johnstone, H.J.H., Prange, M., Steph, S., Groeneveld, J., Mulitza, S., Mackensen, A., 2011. Sea surface temperature reconstruction based on the Mg/Ca ratio of planktonic foraminifera Globigerinoides ruber pink in sediment profile GeoB9526. PANGAEA.
Zarriess, M., Mackensen, A., 2011. Testing the impact of seasonal phytodetritus deposition on δ^{13}C of epibenthic foraminifer *Cibicidoides wuellerstorfi*: A 31,000 year high-resolution record from the northwest African continental slope. Paleoceanography 26 (2), PA2202. https://doi.org/10.1029/2010PA001944.
Zarriess, M., Mackensen, A., 2010. The tropical rainbelt and productivity changes off northwest Africa: A 31,000-year high-resolution record. Mar. Micropaleontol. 76 (3–4), 76–91. https://doi.org/10.1016/j.marmicro.2010.06.001.
Zenk, W., Klein, B., Schroder, M., 1991. Cape Verde Frontal Zone. Deep Sea Research Part A. Oceanographic Research Papers 38, S505–S530. https://doi.org/10.1016/S0198-0149(12)80022-7.
[dataset] Zhao, M., Beveridge, N.A.S., Shackleton, N.J., Sarnthein, M., Eglinton, G., 1995. Eastern Tropical Atlantic Alkenones and Sea Surface Temperatures. NOAA/WDS Paleoclimatology. https://doi.org/10.25921/E4ES-4V37.